



# NAVAL POSTGRADUATE SCHOOL

MONTEREY, CALIFORNIA

## THESIS

**DEVELOPMENT OF NANOPOROUS CARBIDE-DERIVED  
CARBON ELECTRODES FOR HIGH-PERFORMANCE  
LITHIUM-ION BATTERIES**

by

Kamryn M. Sakamoto

September 2011

Thesis Advisor:

Sebastian Osswald

Second Reader:

Joseph C. Farmer

**Approved for public release; distribution is unlimited**

THIS PAGE INTENTIONALLY LEFT BLANK

REPORT DOCUMENTATION PAGE			Form Approved OMB No. 0704-0188	
Public reporting burden for this collection of information is estimated to average 1 hour per response, including the time for reviewing instruction, searching existing data sources, gathering and maintaining the data needed, and completing and reviewing the collection of information. Send comments regarding this burden estimate or any other aspect of this collection of information, including suggestions for reducing this burden, to Washington headquarters Services, Directorate for Information Operations and Reports, 1215 Jefferson Davis Highway, Suite 1204, Arlington, VA 22202-4302, and to the Office of Management and Budget, Paperwork Reduction Project (0704-0188) Washington DC 20503.				
1. AGENCY USE ONLY (Leave blank)		2. REPORT DATE September 2011	3. REPORT TYPE AND DATES COVERED Master's Thesis	
4. TITLE AND SUBTITLE Development of Nanoporous Carbide-Derived Carbon Electrodes for High-Performance Lithium-Ion Batteries			5. FUNDING NUMBERS	
6. AUTHOR(S) Kamryn M. Sakamoto				
7. PERFORMING ORGANIZATION NAME(S) AND ADDRESS(ES) Naval Postgraduate School Monterey, CA 93943-5000			8. PERFORMING ORGANIZATION REPORT NUMBER	
9. SPONSORING /MONITORING AGENCY NAME(S) AND ADDRESS(ES) N/A			10. SPONSORING/MONITORING AGENCY REPORT NUMBER	
11. SUPPLEMENTARY NOTES The views expressed in this thesis are those of the author and do not reflect the official policy or position of the Department of Defense or the U.S. Government. IRB Protocol number ____N/A____.				
12a. DISTRIBUTION / AVAILABILITY STATEMENT Approved for public release; distribution is unlimited			12b. DISTRIBUTION CODE	
13. ABSTRACT (maximum 200 words) Lithium ion batteries are the state-of-the-art power sources for portable electronic devices and, due to their superior energy and power densities, are promising candidates for the demanding energy storage applications of the U.S. Navy and other branches of the military. While graphitic carbon is currently the most common anode material in lithium ion batteries, it suffers from low specific capacity (~372 mAh/g) and poor power characteristics. In contrast, amorphous carbons allow for faster charge/discharge kinetics and were found to exhibit specific capacities of up to 1000 mAh/g due to a different, and still unknown storage mechanism.  This work examines the suitability of amorphous carbide-derived carbon (CDC) anodes for high-power and high-energy density lithium ion batteries. Using different material characterization techniques, such as Raman Spectroscopy, X-Ray Diffraction (XRD), and Scanning Electron Microscope (SEM), we aim to determine the relationship between the structural features of CDC to its electrochemical performance. Studies were conducted on three titanium carbide (TiC)-based CDC powders, synthesized at 600, 1000, and 1200 °C. Custom-made CDC anodes were fabricated, tested and cycled against commercial LiCoO2 and lithium metal cathodes in button-type coin cell enclosures. Electrochemical testing revealed specific capacities approaching 300 mAh/g. While the observed specific energy is lower than that of a conventional graphite anodes, the results are promising and may provide deeper insights into the relatively unknown charge storage mechanism in amorphous carbons. Our results also indicate that CDCs allow for substantial improvements in power characteristics, but additional research is needed to verify the obtained results and further optimize the electrode fabrication process.				
14. SUBJECT TERMS Lithium-Ion Batteries, Amorphous Carbon, Carbide-Derived Carbon, Raman Spectroscopy, X-Ray Diffraction, Scanning Electron Microscope			15. NUMBER OF PAGES 93	
			16. PRICE CODE	
17. SECURITY CLASSIFICATION OF REPORT Unclassified	18. SECURITY CLASSIFICATION OF THIS PAGE Unclassified	19. SECURITY CLASSIFICATION OF ABSTRACT Unclassified	20. LIMITATION OF ABSTRACT UU	

THIS PAGE INTENTIONALLY LEFT BLANK

**Approved for public release; distribution is unlimited**

**DEVELOPMENT OF NANOPOROUS CARBIDE-DERIVED CARBON  
ELECTRODES FOR HIGH-PERFORMANCE LITHIUM-ION BATTERIES**

Kamryn M. Sakamoto  
Lieutenant, United States Navy  
B.S., United States Naval Academy, 2007

Submitted in partial fulfillment of the  
requirements for the degree of

**MASTER OF SCIENCE IN MECHANICAL ENGINEERING**

from the

**NAVAL POSTGRADUATE SCHOOL  
September 2011**

Author: Kamryn M. Sakamoto

Approved by: Sebastian Osswald  
Thesis Advisor

Joseph C. Farmer  
Second Reader

Knox T. Millsaps  
Chair, Department of Mechanical and Aerospace  
Engineering

THIS PAGE INTENTIONALLY LEFT BLANK

## ABSTRACT

Lithium ion batteries are the state-of-the-art power sources for portable electronic devices and, due to their superior energy and power densities, are promising candidates for the demanding energy storage applications of the U.S. Navy and other branches of the military. While graphitic carbon is currently the most common anode material in lithium ion batteries, it suffers from low specific capacity (~372 mAh/g) and poor power characteristics. In contrast, amorphous carbons allow for faster charge/discharge kinetics and were found to exhibit specific capacities of up to 1,000 mAh/g due to a different, and still unknown, storage mechanism.

This work examines the suitability of amorphous carbide-derived carbon (CDC) anodes for high-power and high-energy density lithium ion batteries. Using different material characterization techniques, such as Raman Spectroscopy, X-Ray Diffraction (XRD), and Scanning Electron Microscope (SEM), we aim to determine the relationship between the structural features of CDC to its electrochemical performance. Studies were conducted on three titanium carbide (TiC)-based CDC powders, synthesized at 600, 1,000, and 1,200 °C. Custom-made CDC anodes were fabricated, tested and cycled against commercial  $\text{LiCoO}_2$  and lithium metal cathodes in button-type coin cell enclosures. Electrochemical testing revealed specific capacities approaching 300 mAh/g. While the observed specific energy is lower than that of a conventional graphite anodes, the results are promising and may provide deeper insights into the relatively unknown charge storage mechanism in amorphous carbons. Our results also indicate that CDCs allow for substantial improvements in power characteristics, but additional research is needed to verify the obtained results and further optimize the electrode fabrication process.

THIS PAGE INTENTIONALLY LEFT BLANK

# TABLE OF CONTENTS

I.	INTRODUCTION.....	1
A.	ENERGY STORAGE.....	1
B.	LI-ION BATTERY DESIGN.....	9
1.	Cathode Materials.....	13
2.	Electrolytes.....	15
3.	Anode Materials.....	17
C.	CARBON ANODES.....	18
1.	Graphite.....	20
2.	Soft Carbons.....	21
3.	Hard Carbons.....	22
4.	Carbide-Derived Carbon.....	24
5.	Synthesis.....	24
6.	Structure and Properties.....	26
7.	Application in Energy Storage.....	27
D.	THESIS OBJECTIVES.....	28
II.	EXPERIMENTAL SECTION.....	31
A.	MATERIALS.....	31
B.	CHARACTERIZATION METHODS.....	32
1.	X-Ray Diffraction.....	32
2.	Scanning Electron Microscopy.....	33
3.	Raman Spectroscopy.....	34
C.	MACCOR BATTERY TESTER.....	36
III.	RESULTS AND DISCUSSION.....	37
A.	ELECTRODE PRODUCTION.....	37
1.	Electrode Powder Preparation.....	37
2.	Slurry Preparation and Electrode Casting.....	39
B.	ELECTRODE CHARACTERIZATION.....	46
1.	X-Ray Diffraction Results.....	46
2.	Raman Spectroscopy.....	47
3.	Scanning Electron Microscopy.....	52
C.	ELECTRODE AND BATTERY TESTING.....	53
1.	Graphite Anodes.....	54
2.	Carbide-Derived Carbon Anodes.....	60
IV.	SUMMARY AND CONCLUSIONS.....	69
	LIST OF REFERENCES.....	71
	INITIAL DISTRIBUTION LIST.....	73

THIS PAGE INTENTIONALLY LEFT BLANK

## LIST OF FIGURES

Figure 1.	Ragone plot compares the performance of a range of electrochemical devices. It shows that ultracapacitors (supercapacitors) can deliver very high power but storage capacity is very limited. On the other end, fuel cells can store large amounts of energy but have a relatively low power output. Lithium ion batteries have relatively high energy density and considerable power density (From [3]).	7
Figure 2.	Charge-discharge mechanism of Li-ion battery. The chemical reactions and the flow of electrons are shown during the charge-discharge mechanism (From [6]).	10
Figure 3.	Structure of practical Li-ion cell. The main components are shown of a cylindrical Li-ion battery (From [7]).	11
Figure 4.	Intercalation of lithium ions into anode and cathode host lattices during charge and discharge of a Li-ion battery. Lithium ions are reversibly removed from or inserted into a host lattice without considerable change to the structure of the host.	12
Figure 5.	Voltage vs. capacity plot (second cycle) of three different carbon anodes: synthetic graphite (region A), soft carbon derived from petroleum pitch at 500 °C (region B), and hard carbon from resole resin heat-treated at 1000 °C (region C). Lithium metal is used as reference and counter electrode (From [7]).	21
Figure 6.	Specific charge capacity of the various kinds of carbon fiber and PPP-based carbon electrodes at the second cycle as a function of crystallite thickness, $L_{C(002)}$ , determined by X-ray diffraction analysis. Dahn et al. also proposed three regions of lithium insertion capacity by the heat treatment temperatures of carbon materials (From [8]).	23
Figure 7.	(a) High-resolution transmission electron microscopy (HRTEM) image of metal carbide before and after chlorination. (b) Schematic illustrating the importance of precursor material on final CDC structure (From [11]).	25
Figure 8.	XRD of TiC and TiC-CDC samples synthesized at different temperatures. Complete conversion of TiC to carbon takes place at 400°C and above. Broad peaks show the highly amorphous nature of the carbon produced from TiC (From [10]).	27
Figure 9.	LiFePO <sub>4</sub> , acetylene black, and PVDF powders in weighing boat before mixing.	38
Figure 10.	The 8000 M SPEX Sample Prep Mixer/Mill used to ball mill anode or cathode powders together with acetylene black and PVDF binder.	38
Figure 11.	a) Slurry preparation setup under the fume hood with NMP solvent, glass pipette with dispenser, and the ball milled powder mixture	

	containing LiFePO <sub>4</sub> , acetylene black, and PVDF binder; and b) Prepared slurry after adding NMP solvent to the powder mixture. ....	39
Figure 12.	Sample vial containing a LiFePO <sub>4</sub> slurry inside the ultrasonic bath. Each vial was sonicated for 30 minutes.....	41
Figure 13.	Aluminum foil current collector taped on a glass plate. The foil was flattened with Kim wipes and ethanol. ....	41
Figure 14.	(a) LiFePO <sub>4</sub> slurry laid onto foil current collector and (b) LiFePO <sub>4</sub> slurry casted with applicator and (c) LiFePO <sub>4</sub> casted. ....	42
Figure 15.	(a) LiFePO <sub>4</sub> dried film with cracks and flakes and (b) LiFePO <sub>4</sub> dried film and (c) TiC CDC 600 °C film.....	43
Figure 16.	Disk-shaped TiC CDC 600°C coin-cell anodes were punched out from dried electrode films. ....	43
Figure 17.	An Argon-filled glove box was used to prepare and assemble the coin cell batteries. The glove box prevents the electrodes from getting in contact with oxygen and moisture, both of which are known to reduce the cycle-life of Li-ion batteries.....	44
Figure 18.	Button-type coin cell assembly schematic. ....	45
Figure 19.	X-ray diffraction pattern of TiC-CDC synthesized 600, 1000, 1200°C, in comparison to data collected from nanocrystalline graphite. ....	46
Figure 20.	Raman Spectra of TiC CDC 600°C taken at five random sample spots. Raman spectra were recorded using 514 nm laser excitation..	48
Figure 21.	Raman Spectra of TiC-CDC 1000 °C taken at five random spots on the sample. ....	49
Figure 22.	Raman Spectra of TiC-CDC 1200°C taken at five different random spots on the sample. ....	50
Figure 23.	Raman Spectra of TiC-CDC 600, 1000, and 1200 °C. The peak width of the D and G bands decreases with increasing synthesis temperature indicating higher order and graphitization.....	51
Figure 24.	SE SEM images of TiC-CDC 600°C (a) and TiC-CDC 1000°C (b) electrodes at a magnification of 500X.....	52
Figure 25.	SE SEM images of TiC-CDC 600°C (a) and TiC-CDC 1000°C (b) electrodes at a magnification of 5000X.....	53
Figure 26.	SE SEM images of TiC-CDC 600°C (a) and TiC-CDC 1000°C (b) electrodes at a magnification of 25kX.....	53
Figure 27.	Charge and discharge behavior of a graphite/ LiCoO <sub>2</sub> coin cell during the (a) first and (b) fifth cycles. The charge and discharge current was 0.361 mA, which corresponds to a C-rate of ~C/12. ....	55
Figure 28.	Specific charge and discharge capacities of a graphite/ LiCoO <sub>2</sub> coin cell during the first five cycles. The charge and discharge current was 0.36 mA (C/12).....	55
Figure 29.	Specific charge and discharge capacities of a graphite/ LiCoO <sub>2</sub> coin cell at difference charge/discharge rates (rate testing). A C-rate of 1C corresponds to a current of 4mA.....	57

Figure 30.	Cell voltage of a graphite/ Li metal coin cell during charge and discharge in the first (a) and fifth (b) cycles. The cell was charged and discharge at current of 0.361 mA (C/12).....	58
Figure 31.	Specific charge and discharge capacity of graphite/ Li Metal half-cell as a function of cycle number. The charge and discharge current was set to 0.36 mA (C/12).....	58
Figure 32.	Specific charge and discharge capacities of a graphite/ Li metal coin cell at difference charge/discharge rates (rate testing). A C-rate of 1C corresponds to a current of 4 mA.....	59
Figure 33.	Cell voltage of a TiC-CDC 600°C/LiCoO <sub>2</sub> coin cell during charge and discharge in the first (a) and fifth (b) cycles. The cell was charged and discharge at current of 0.30 mA (C/5).....	60
Figure 34.	Specific charge and discharge capacity of a TiC-CDC 600°C/ LiCoO <sub>2</sub> coin cell as a function of cycle number. The charge and discharge current was set to 0.30 mA (C/5). ....	61
Figure 35.	Cell voltage of a TiC CDC 600°C/Li metal coin cell during charge and discharge in the first (a) and fourth (b) cycles. The cell was charged and discharge at current of 0.30 mA (C/8).....	62
Figure 36.	Specific charge and discharge capacity of a TiC CDC 600°C/ Li metal coin cell as a function of cycle number. The charge and discharge current was set to 0.30 mA (C/8). ....	62
Figure 37.	Specific charge and discharge capacity of a TiC CDC 600°C/ Li metal coin cell as a function of cycle number. The charge and discharge current was set to 0.30 mA (C/7). ....	63
Figure 38.	Cell voltage of a TiC-CDC 1000°C/Li metal coin cell during charge and discharge in the first (a) and fifth (b) cycles. The cell was charged and discharge at current of 0.30 mA (C/8).....	64
Figure 39.	Specific charge and discharge capacity of a TiC-CDC 1000°C/ Li metal coin cell as a function of cycle number. The charge and discharge current was set to 0.30 mA (C/8). ....	64
Figure 40.	Cell voltage of a TiC-CDC 1200°C/LiCoO <sub>2</sub> coin cell during charge and discharge in the first (a) and fifth (b) cycles. The cell was charged and discharge at current of 0.30 mA (C/2).....	65
Figure 41.	Specific charge and discharge capacity of a TiC-CDC 1200°C/ LiCoO <sub>2</sub> coin cell as a function of cycle number. The charge and discharge current was set to 0.30 mA (C/2). ....	65
Figure 42.	Cell voltage of a TiC-CDC 1200°C/Li metal half-cell during charge and discharge in the first (a) and fifth (b) cycles. The cell was charged and discharge at current of 0.30 mA (1C).....	66
Figure 43.	Specific charge and discharge capacity of a TiC-CDC 1200°C/ Li metal half-cell as a function of cycle number. The charge and discharge current was set to 0.30 mA (1C). ....	67

THIS PAGE INTENTIONALLY LEFT BLANK

## LIST OF TABLES

Table 1.	Major characteristics and applications of primary batteries. Major advantages of the primary battery are convenience, simplicity, ease of use, requires little to no maintenance, good-shelf life, reasonable energy, power density, reliability, and acceptable cost (From [2]).	3
Table 2.	Major characteristics and applications of secondary batteries. Important characteristics of the secondary battery are that charge and discharge proceed nearly reversibly, energy efficient and has minimal physical changes that can limit cycle life (From [2]).	5
Table 3.	Required characteristic of Li-ion battery cathode materials. These requirements primarily guide the selection and development of new cathode materials (From [2]).	13
Table 4.	Characteristics of common cathode materials with layered or spinel-type lattice structure (From [2]).	14
Table 5.	Properties and performance of various carbons. An ideal carbon material would offer high specific capacity without irreversible capacity (From [2]).	19
Table 6.	Carbide-derived carbon precursors for synthesizing CDC materials (From [12]).	26
Table 7.	Optimized recipes of different electrode mixtures listing the amounts of active material, acetylene black, PVDF binder and NMP solvent.	40

THIS PAGE INTENTIONALLY LEFT BLANK

## LIST OF ACRONYMS AND ABBREVIATIONS

BSE	Backscattered Electrons
CDC	Carbide Derived Carbon
CRT	Cathode-Ray Tube
DEC	Diethyl Carbonate
DMC	Dimethyl Carbonate
EC	Ethylene Carbonate
EMC	Ethyl Methyl Carbonate
eV	Electron Volt
Li	Lithium
LiCoO <sub>2</sub>	Lithium Cobalt Oxide
Li-ion	Lithium ion
NMP	N-Methyl-2-Pyrrolidone
PC	Propylene Carbonate
PVDF	Polyvinylidene Fluoride
SE	Secondary Electrons
SEI	Solid Electrolyte Interphase
SEM	Scanning Electron Microscopy
TiC	Titanium Carbide
UV	Ultraviolet
V	Volt
XRD	X-Ray Diffraction
Z	Atomic Weight

## LIST OF SYMBOLS

Å	Angstrom
Ar	Argon

THIS PAGE INTENTIONALLY LEFT BLANK

## ACKNOWLEDGMENTS

First and foremost, I would like to thank my thesis advisor, Dr. Sebastian Osswald. Being his first student, I spent much time assisting Dr. Osswald in setting up his new laboratories at NPS, in addition to a heavy course load and time-consuming experimental thesis research. Despite the long and challenging thesis process, Dr. Osswald was always there to guide and help me the entire way. I greatly appreciate his tireless efforts and his dedication when working with me toward this major milestone in my life.

I would also like to thank my co-advisor, Dr. Joseph Farmer. His wealth of knowledge and dedication to teaching significantly contributed to the successful completion of this thesis. I appreciate all the time and the support that Dr. Farmer provided, both inside and outside of the classroom.

Special thanks goes to Dr. Luke Brewer for all his help related to the radiation safety training. Dr. Brewer was also my professor for one of my 4000-level materials science courses, which aided tremendously in my thesis research. Dr. Sarath Menon also made significant contributions to my thesis, training me how to use both the XRD and SEM. He also taught two 4000-level materials science courses that helped me on my research. Additionally, I would like to thank Dr. Chanman Park for always being around to help when problems occurred with the XRD. Mr. Sam Barone deserves acknowledgement for supplying the deionized water for the lab. Lastly, I would like to show appreciation for Ms. Sandra Stephens' help with routing my proposal and helping with the administrative work. Thank you to all mentioned above—if it was not for all of your help, I would have never been able to finish my thesis and I am extremely grateful.

THIS PAGE INTENTIONALLY LEFT BLANK

# I. INTRODUCTION

## A. ENERGY STORAGE

Energy has moved to the center of current discussions on national security, U.S. foreign policy, and environmental concerns. Due to the advancing depletion of natural resources and increasing levels of environmental pollution of Earth's oceans and atmosphere, energy-efficient technologies are in an ever-growing demand. In the wake of the energy challenges facing our and future generations, researchers are focusing on new ways to enhance the utilization of renewable energy sources and reduce our dependence on fossil fuels. However, with the increasing reliance on green energy comes the need for advanced energy storage technologies that are able to balance differences between the electricity demand of our communities and the fluctuating supply from alternative energy sources, such as solar and wind. Therefore, energy storage plays a vital and increasing role in our daily lives, and is of rapidly increasing importance to the U.S. Navy and other branches of our military.

Over the past decades, the Navy has utilized a variety of different energy storage technologies to power its naval platforms and weapon systems. Typically, one distinguishes between two basic forms of energy storage: mechanical energy storage and electrical (electrochemical and capacitive) energy storage. Mechanical energy storage systems convert electrical energy to mechanical energy, which is stored, and are typically used when a surplus of cheap off-peak electricity is available. There are three primary types of mechanical energy storage systems: 1) flywheel energy storage (FES), 2) pumped hydropower storage (PHS), and 3) compressed-air energy storage (CAES) [1]. Electrochemical and capacitive energy storage systems use chemical reactions and charge carrier separation mechanisms, respectively, to store electrical energy. Electrochemical energy storage devices are primary and

secondary battery systems. In contrast, capacitors and supercapacitors store electricity by separating anion and cations using large surface area electrodes.

Batteries are comprised of several functional components: anode, cathode, electrolyte, separator, and containment. As batteries are charged, an external voltage is applied across the electrodes and drives the chemical reactions at the anode and cathode. During discharge, the chemical reactions run in reverse and electrons flow through an external circuit thus providing electrical energy. Some of the advantages of electrochemical and capacitive energy storage devices over mechanical systems include high efficiency, flexibility, and versatility [1].

There exists a vast range of both primary and secondary battery systems. Primary batteries are non-rechargeable while secondary batteries are rechargeable. Common primary batteries are zinc-carbon, zinc-alkaline-manganese dioxide, zinc-silver oxide, zinc-air batteries, and lithium-air batteries [2]. Secondary batteries comprise of lead-acid, silver-zinc, nickel cadmium, nickel-metal hydride, lithium-ion, sodium-beta, nickel-hydrogen, and regenerative fuel cells.

Primary batteries are the energy source of choice for a variety of portable consumer electronics. General applications include, but are not limited to, lighting, PDA's (Personal Digital Assistant), communication devices, hearing aids, toys and watches. The major advantages of primary batteries are its ease of use, low maintenance, simplicity, convenience, flexibility, reasonable energy, considerable power density, reliability, good shelf life, and acceptable cost [2]. An overview of the most common primary battery chemistries and their characteristics is given in Table 1.

System	Characteristics	Applications	Energy Density (Wh/L)
Zinc-carbon (Leclanche) Zinc/MnO <sub>2</sub>	Common, low-cost primary battery; available in a variety of sizes	Flashlight, portable radios, toys, novelties, instruments	Low
Magnesium (Mg/MnO <sub>2</sub> )	High-capacity primary battery; long shelf life	Military receiver-transmitters, aircraft emergency transmitters	High
Mercury (Zn/HgO)	Highest capacity (by volume) of conventional types; flat discharge; good shelf life	Hearing aids, medical devices (pacemakers), photography, detectors, military equipment but in limited use due to environmental hazard of mercury	470
Mercad (Cd/HgO)	Long shelf life; good low- and high-temperature performance; low energy density	Special applications requiring operation under extreme temperature conditions and long life; in limited use	Low
Alkaline (Zn/alkaline/MnO <sub>2</sub> )	Most popular general-purpose premium battery; good low-temperature and high-rate performance; moderate cost	Most popular primary-battery; used in a variety of portable battery operated equipments	360
Silver/zinc (Zn/Ag <sub>2</sub> O)	Highest capacity (by weight) of conventional types; flat discharge; good shelf life, costly	Hearing aids, photography, electric watches, missiles, underwater and space application (larger sizes)	575
Zinc/air (Zn/O <sub>2</sub> )	Highest energy density, low cost; not independent of environmental conditions	Special applications, hearing aids, pagers, medical devices, portable electronics	1450
Lithium/soluble cathode	High energy density; long shelf life; good performance over wide temperature range	Wide range of applications (capacity from 1 to 10,000 Ah) requiring high energy density, long shelf life, e.g., from utility meters to military power applications	400
Lithium/solid cathode	High energy density; good rate capability and low-temperature performance; long shelf life; competitive cost	Replacement for conventional button and cylindrical cell applications	High
Lithium/solid electrolyte	Extremely long shelf life; low-power battery	Medical electronics, memory circuits, fusing	Low

Table 1. Major characteristics and applications of primary batteries. Major advantages of the primary battery are convenience, simplicity, ease of use, requires little to no maintenance, good-shelf life, reasonable energy, power density, reliability, and acceptable cost (From [2]).

Secondary or rechargeable batteries are currently being used in starting, lighting, and ignition (SLI) automotive applications, both emergency and standby power, and industrial truck materials-handling equipment. Smaller secondary batteries are also used in portable devices, such as toys, tools, lighting, radio, laptop computers, and cell phones. During recent years, researchers have

focused their efforts on developing secondary battery systems for electrical and hybrid electric vehicles. Applications of secondary batteries can be grouped into two categories: 1. Applications used as an energy storage device, such as automotive systems, standby power sources, and hybrid devices. 2. Applications where the secondary battery is discharged and recharged after use, such as consumer electronics, electric-vehicles, and industrial trucks. The replacement of primary cells by secondary batteries is for increased convenience, cost reduction, and improved power capabilities [2]. Table 2 summarizes the most common secondary battery technologies.

System	Characteristics	Applications	Energy Density (Wh/L)
<b>Lead-acid:</b>			
Automotive	Popular, low-cost secondary battery, moderate specific-energy, high rate, and low-temperature performance; maintenance-free designs	Automotive SLI, golf carts, lawn mowers, tractors, aircraft, marine	70
Traction (motive power)	Designed for deep 6-9 h discharge, cycling service	Industrial trucks, materials handling, electric and hybrid electric vehicles, special types for submarine power	80
Stationary	Designed for standby float service, long life, VRLA designs	Emergency power, utilities, telephone, UPS, load leveling, energy storage, emergency lighting	50-70
Portable	Sealed, maintenance-free, low cost, good float capability, moderate cycle life	Portable tools, small appliances and devices, TV and portable electronic equipment	90
<b>Nickel-cadmium:</b>			
Industrial and FNC	Good high-rate, low-temperature capability, flat voltage, excellent cycle life	Aircraft batteries, industrial and emergency power applications, communication equipment	15-80
Portable	Sealed, maintenance-free, good high-rate low-temperature performance, excellent cycle life	Railroad equipment, consumer electronics, portable tools, pagers, appliances, and photographic equipment, standby power, memory backup	100
Nickel-metal hydride	Sealed, maintenance-free, higher capacity than nickel-cadmium batteries	Consumer electronics and other portable applications; electric and hybrid electric vehicles	240
Nickel-iron	Durable, rugged construction, long life low specific energy	Materials handling, stationary applications, railroad cars	55
Nickel-zinc	High specific energy, extended cycle life and rate capability	Bicycles, scooters, trolling motors	80-120
Silver-zinc	Highest specific energy, very good high-rate capability, low cycle life, high cost	Lightweight portable electronic and other equipment; training targets, drones submarines, other military equipment, launch vehicles and space probes	180
Silver-cadmium	High specific energy, good charge retention, moderate cycle life, high cost	Portable equipment requiring a lightweight, high-capacity battery; space satellites	120
Nickel-hydrogen	Long cycle life under shallow discharge, long life	Primarily for aerospace applications such as LEO and GEO satellites	105
Ambient-temperature rechargeable "primary" types [Zn/MnO <sub>2</sub> ]	Low cost, good capacity retention, sealed and maintenance-free, limited cycle life and rate capability	Cylindrical cell applications, rechargeable replacement for zinc-carbon and alkaline primary batteries, consumer electronics (ambient-temperature systems)	250
Lithium ion	High specific energy and energy density, long cycle life	Portable and consumer electronic equipment electric vehicles, and space applications	400

Table 2. Major characteristics and applications of secondary batteries. Important characteristics of the secondary battery are that charge and discharge proceed nearly reversibly, energy efficient and has minimal physical changes that can limit cycle life (From [2]).

In order to compare the tradeoffs between specific energy (energy per unit mass, Wh/kg) and specific power (power per unit mass, W/kg), or the tradeoffs between energy density and power density for various energy storage

technologies, Ragone charts are used (Figure 1). This chart provides an excellent means to compare diverse energy storage technologies, ranging from capacitors to batteries and fuel cells. On the upper left end of the plot, fuel cells have extremely high energy densities, but exhibit poor power characteristic. In other words, fuel cells can store a lot of energy, but the energy cannot be accessed rapidly. In contrast, aluminum-electrolytic capacitors (lower right corner) have high power output, but are subject to low energy densities. Capacitors store less energy than batteries and fuel cells, but the available energy can be accessed almost instantaneously. The diagonal lines in Figure 1 represent the relative time to get the charge into or out of the particular device. At the left end of the plot power can be taken out or put into capacitors in a matter of microseconds. This makes capacitors ideal candidates for applications in regenerative braking in electric vehicles or to power emergency actuation systems for doors and evacuation slides in airliners. In contrast, fuel cells have poor dynamic performance as it takes them hours to generate and deliver their energy. Due to the complementary nature of these devices, capacitors and fuel cells are often times used together to take advantage of their individual strengths and overcome their weaknesses. Li-ion batteries are in the middle indicating a reasonable compromise between power and energy density.

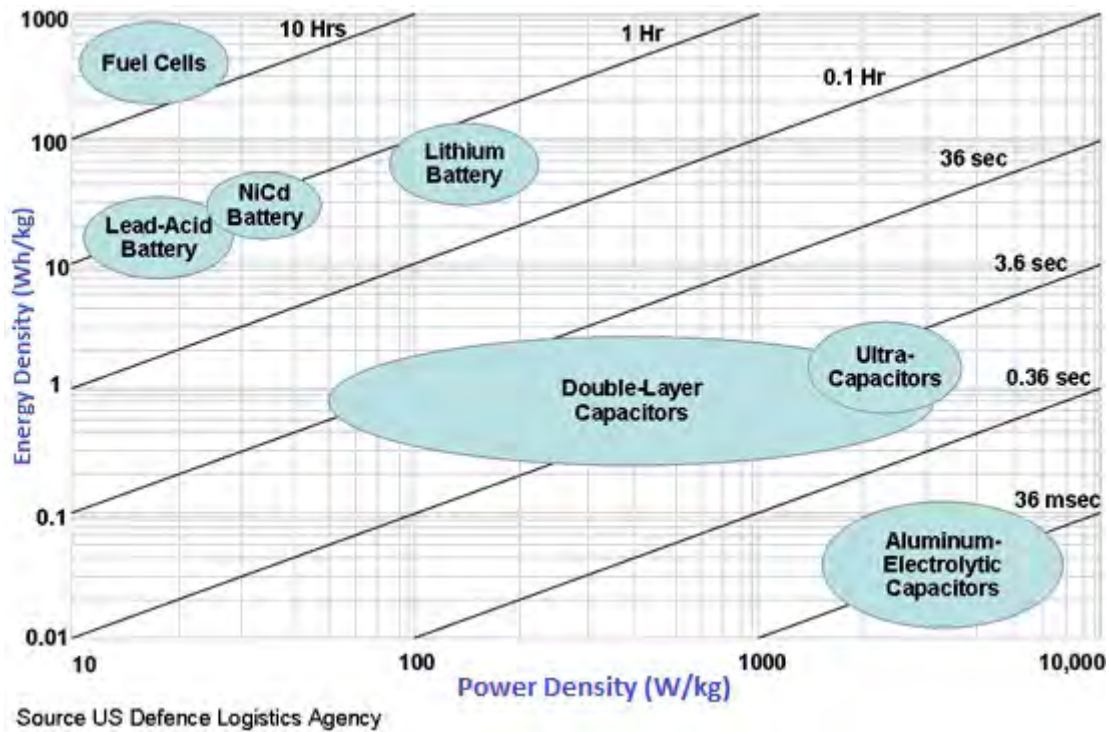


Figure 1. Ragone plot compares the performance of a range of electrochemical devices. It shows that ultracapacitors (supercapacitors) can deliver very high power but storage capacity is very limited. On the other end, fuel cells can store large amounts of energy but have a relatively low power output. Lithium ion batteries have relatively high energy density and considerable power density (From [3]).

For both primary and secondary batteries, there exists a wide variety of different anode and cathode materials. The performance of the battery (e.g., voltage, power density, energy density, temperature stability, cycle life, etc.) depends on the characteristics of the anode and cathode. The electrode materials are often compared on the basis of their specific capacity, half-cell voltages, and the specific energy of devices that incorporate them as electrode materials. Hydrogen and lithium are very light elements, and therefore have very high specific capacities, and enable cells to be built with very high specific energy. Due to their great potential for energy applications, both hydrogen fuel cells and lithium-based batteries are among the most promising technologies in in the energy storage field [4]. Oxygen is the most energy dense cathode

material. Although oxygen can be extracted from the atmosphere, in underwater situations such as a submarine, it must be stored making it more challenging to design an energy storage system for underwater applications [4]. Despite the simplicity of finding the most energy dense anode and cathode materials for energy storage devices, this combination does not necessarily create the best performing battery. Important factors in determining the power and energy characteristics are also the compatibility of the anode and cathode materials, and the reversibility of the chemical reactions of the systems [4].

Zinc-carbon batteries have been used for over 100 years and, until recently, were the most popular type of primary cell due their low cost and reliable performance. However, recent advances in battery technology led to the development of superior primary batteries. One of the most common primary cell today is the alkaline (Zn/MnO<sub>2</sub>) battery. Alkaline batteries are notorious for their excellent performance at high currents and lower temperatures as well as an exceptionally long shelf life [2]. These batteries are currently the energy source of choice for cameras and other consumer electronics requiring high power capability. Silver/zinc batteries have a higher energy density than the similar zinc/mercuric oxide cells and slightly better performance characteristics. Because of the high cost of silver/zinc cells, this type of battery is limited to powering small devices, such as hearing aids. The zinc/air battery has one of the highest energy density as no solid cathode material is needed; however, its weakness has been sensitivity to extreme temperatures and other environmental factors. Because of the high energy density of zinc/air and other metal/air batteries further research is being conducted in this area. Finally, lithium batteries have the highest energy density, can operate over a vast temperature range, and exhibit good shelf life. On the downside, they are still subject to high cost and safety issues, and have yet not overtaken the battery market. However, the great potential seen in lithium-based batteries has paved the way for the development of the Li-ion battery technology [2].

Lead-acid batteries are the most common secondary battery technology for automotive applications and large-scale electrochemical energy storage systems, including energy storage aboard submarines and uninterruptible power supplies (UPS). Due to the versatility of this technology, there exist several different types of cell designs, depending on the particular application (Table 2). Although the lead-acid cell is one of the older battery technologies, it is one of the most popular because of its high reliability over a wide temperature range, low cost, good performance, and respectable cycle life. The most common alkaline secondary battery is the nickel-cadmium cell. Nickel-cadmium batteries come in different sizes and shapes, and are available in industrial and portable forms (Table 2). The main advantages are high durability, the ability to handle both mechanical and electrical abuse, and low maintenance requirements, making nickel-cadmium cell the battery of choice for industrial work environments [2]. The silver-zinc or silver oxide secondary battery is known for its high specific energy, low internal resistance, flat second discharge plateau, and high specific power, rendering it particularly useful for military applications (e.g., submarines) [2]. Limitations include the high cost of the active material (silver), relatively low cycle life (perhaps as low as 100 charge-discharge cycles to 80% of the initial capacity), and poor performance at low temperatures [2]. Finally, Li-ion batteries have entered the secondary battery market and are now the storage technology of choice for portable consumer electronics, such as laptop computers, cell phones and camcorders. The excellent performance of Li-ion cells are noted by their high energy density, high specific energy, and long cycle life (greater than 1000 cycles at 80% depth of discharge) [2].

## **B. LI-ION BATTERY DESIGN**

The development of rechargeable Li-ion batteries dates back to the late 1970s. The idea of using lithium metal as an anode material is based on the fact that it is the most electropositive ( $-3.04$  V versus the standard hydrogen electrode) and lightweight solid material (molar mass =  $6.94$  g/mol and specific

gravity = 0.53 g/cm<sup>3</sup>) [5]. While metallic lithium exhibits several favorable physical and chemical characteristics and became an attractive electrode material for use in energy storage, safety concerns linked to the chemical reactivity and the fire hazard have sparked the development of intercalation anodes, particular carbon-based electrodes. The intercalation of lithium ions in a carbon host structure is inherently safer than the use of lithium metal. A schematic of a common Li-ion battery is shown in Figure 2. Most Li-ion batteries consist of a graphitic carbon anode (negative electrode) and metal oxide cathode, such as LiCoO<sub>2</sub> (positive electrode) [4].

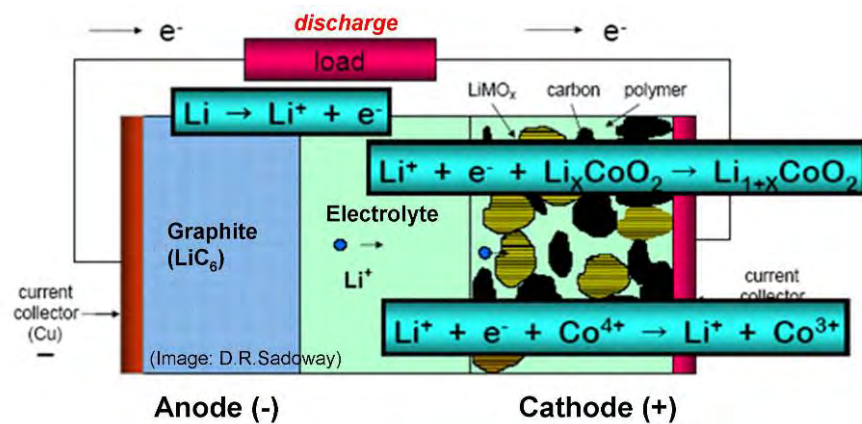


Figure 2. Charge-discharge mechanism of Li-ion battery. The chemical reactions and the flow of electrons are shown during the charge-discharge mechanism (From [6]).

The anode and cathode powders are adhered to a metal foil current collector and held together by polymeric binders, such as polyvinylidene fluoride (PVDF). The current collector foils are different for the anode and cathode, with copper and aluminum being used for the negative (anode) and positive (cathode) electrodes, respectively [4]. Anode and cathode are electrically isolated by an ion-conducting microporous polyethylene (PE) or polypropylene (PP) separator film that is soaked with a liquid electrolyte [2]. More advanced Li-ion battery technologies employ gel-polymer or solid-state electrolytes. [2]

In Figure 3, the components are shown of a Li-ion battery. As displayed, the anode and its current collector are separated by a separator from the cathode and its current collector. In this particular example the Li-ion battery is cylindrical specifically called an 18650, the name based on its dimensions.

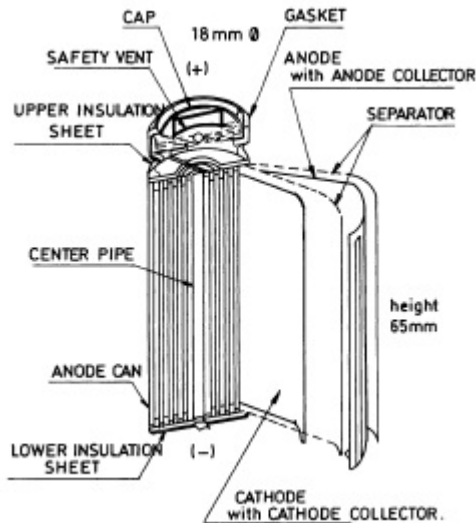


Figure 3. Structure of practical Li-ion cell. The main components are shown of a cylindrical Li-ion battery (From [7]).

These batteries utilize the same anode and cathode materials, but replace the volatile liquid electrolyte with a semi-solid gel-polymer or solid state electrolytes, respectively. Despite their slightly different construction, gel-polymer and conventional Li-ion batteries undergo the same electrochemistry.

Anode and cathode materials typically exhibit a layered or tunneled lattice structure and serve as hosts for the lithium ions during charge and discharge (Figure 4) [4]. The intercalation process is a topotactic reaction where an internal atomic displacement may occur, but both the initial and final lattices are in coherence as the lithium ions are reversibly inserted into or removed from the host without significant structural changes [2].

Common intercalation compounds include graphite and layered silicates, such as talc and clays [2]. The intercalation of electron donors, such as lithium,

and electron acceptors, such as halogens, into graphite has been studied extensively. Alkali metal intercalation of graphite ( $\text{Li}_x\text{C}_6$ ) is particularly important to the field of Li-ion batteries [4]. The shuttling of  $\text{Li}^+$  ions back and forth between the active intercalation compound on the cathode, and that on the anode, is known as the “rocking chair mechanism.”

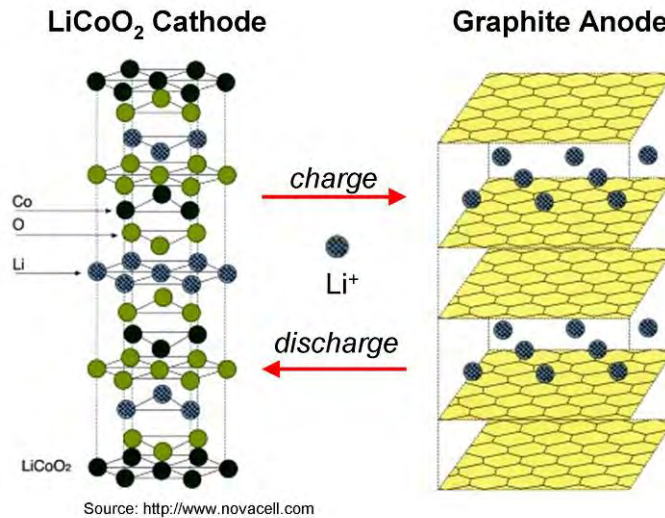
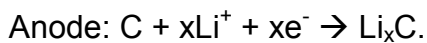
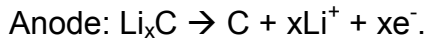
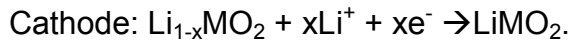


Figure 4. Intercalation of lithium ions into anode and cathode host lattices during charge and discharge of a Li-ion battery. Lithium ions are reversibly removed from or inserted into a host lattice without considerable change to the structure of the host.

As a Li-ion battery is charged, the negative electrode is reduced, while the positive electrode is oxidized:



Note that in this generalized cathode half-cell reaction, “M” denotes a metal such as nickel, cobalt, or manganese, with cobalt being the material of choice in most commercial lithium ion batteries at this point in time [4]. In this charging process, the lithium ions are intercalated into the anode and de-intercalated from the cathode [2]. The exact reverse process occurs upon discharge of the Li-ion battery according to:



Due to the intercalation process, Li-ion cells are safer, less reactive, and have longer cycle life than rechargeable lithium batteries

## 1. Cathode Materials

Cathode materials typically comprise lithiated metal oxides or metal phosphates. The first Li-ion batteries constructed by Goodenough et. al. in 1979 (Sony) employed lithium cobalt oxide ( $\text{LiCoO}_2$ ) cathodes [2]. During the last two decades, a variety of other cathode materials has been developed with the primary goal of utilizing cheaper materials with higher energy densities. In order to be considered a suitable electrode material, potential cathode materials must meet a number of requirements as shown in Table 3.

Requirements for Li-ion Positive Electrode Materials
High free energy of reaction with lithium
Can incorporate large quantities of lithium
Reversibly incorporates lithium without structural change
High lithium ion diffusivity
Good electronic conductivity
Insoluble in the electrolyte
Prepared from inexpensive reagents
Low cost synthesis

Table 3. Required characteristic of Li-ion battery cathode materials. These requirements primarily guide the selection and development of new cathode materials (From [2]).

All of the requirements listed in Table 3 play an important role in the selection of new cathode materials. In order to obtain a high energy density, the lattice of the candidate material must be able to incorporate a large amount of lithium. Additionally, for long cycle life, high coulombic efficiency, and high energy efficiency, the material must reversibly exchange lithium with very little structural

change. For high cell voltage and high energy density, the exchange of lithium at the cathode must take place at a more positive potential with respect to metallic lithium. The electronic and ionic conductivity (Li ion mobility) of the material must also be high since both electrons and ions are exchanged during the charging and discharging processes [4]. The potential cathode material must not be soluble in the electrolyte and must be compatible with the other materials in the battery. Finally, the material must be inexpensive so that Li-ion batteries can be produced on industrial scale with reasonable cost [4].

Commercial cathode materials can be categorized into two different types with either layered or spinel-type lattice structure. Spinel materials have a three-dimensional or tunneled structure. In layered structures like  $\text{LiCoO}_2$  the lithium atoms are intercalated (situated in the space) between the oxygen layers as the cobalt atoms lie within the oxygen octahedral (Figure 4) [2]. On the other hand, in spinel materials such as  $\text{LiMn}_2\text{O}_4$  lithium fills one-eighth of the tetrahedral sites and oxygen octahedra fill one-half of the octahedral sites within the  $\text{LiMn}_2\text{O}_4$  structure. Table 4 shows the voltage and capacity characteristics of common commercially available cathode materials.

Material	Specific Capacity (mAh/g)	Midpoint V vs. Li (at 0.05C)	Advantages or disadvantages
$\text{LiCoO}_2$	155	3.88	Most common commercially, Co is expensive
$\text{LiNi}_{0.7}\text{Co}_{0.3}\text{O}_2$	190	3.7	Intermediate cost
$\text{LiNi}_{0.8}\text{Co}_{0.2}\text{O}_2$	205	3.73	Intermediate cost
$\text{LiNi}_{0.9}\text{Co}_{0.1}\text{O}_2$	220	3.76	Highest specific capacity
$\text{LiNiO}_2$	200	3.55	Most exothermic decomposition
$\text{LiMn}_2\text{O}_4$	120	4	Mn is expensive, low toxicity, least exothermic decomposition

Table 4. Characteristics of common cathode materials with layered or spinel-type lattice structure (From [2]).

The most commonly used cathode material,  $\text{LiCoO}_2$ , has relatively good specific capacity (155 mAh/g) and high half-cell voltage (3.88 V vs. Li) [4]. The

less expensive spinel-type  $\text{LiMn}_2\text{O}_4$  has a lower specific capacity (120 mAh/g), but higher half-cell voltage ( $\sim 4$  V vs. Li), and is used in applications that are either cost sensitive or need excellent cycle stability [4].  $\text{LiNiO}_2$  type cathodes have very high specific capacities (200 mAh/g) and are low cost, but are subject to decomposition, low onset temperatures for thermal runaway, and difficulty of preparation in large quantities [4]. Therefore, despite their high energy density, utilization of  $\text{LiNiO}_2$ -type cathodes is limited (Table 4).

## 2. Electrolytes

There are four different types of electrolytes used in Li-ion batteries: liquid electrolytes, gel electrolytes, polymer electrolytes, and ceramic electrolytes [2]. Liquid electrolytes are usually solutions of lithium salts in organic solvents, such as carbonates. A polymer electrolyte does not contain liquids or solvents, but an ion-conducting phase exists by dissolving salt in a high molecular weight polymer [2]. In contrast, a gel electrolyte is an ion-conducting substance where a salt and solvent are both dissolved or mixed with a high molecular weight polymer [2]. The primary advantage of polymer electrolytes is their increased safety, resulting from low volatility, high viscosity, and lack of a flammable solvent [2]. An advantage of gel electrolytes is that it will enable the battery to be leak free, while providing higher ionic conductivities (better power density) than polymer-based electrolytes [2]. Ceramic electrolytes are also ion-conducting, but comprise inorganic, solid-state materials [2].

Liquid electrolytes are primarily based on organic carbonate solvents, with various lithium salts [4]. The characteristic that makes carbonates particularly suitable for Li-ion batteries is their aprotic, polar, and dielectric nature. These properties allow dissolution of lithium salts at high concentrations ( $>1$  M) and enable compatibility with different electrode materials over a wide potential range [4]. The first organic carbonate solvent used in early Li-ion battery electrolytes was propylene carbonate (PC); however, it was discovered that PC causes exfoliation and degradation of the graphitic anodes during lithium intercalation [2].

Organic carbonate solvents used today include ethylene carbonate (EC), dimethyl carbonate (DMC), ethyl methyl carbonate (EMC), and diethyl carbonate (DEC) [2]. The choice of solvent is influenced by several factors including operation temperature, power requirements, safety, and cost. In common electrolyte formulations, two to four different solvents are mixed together because it allows for improved cell performance, higher conductivity, and operation in a wider temperature range than using only one solvent [2]. EC-based electrolytes exhibit low irreversible capacity and minimal capacity fade when operated with graphitic anodes, but are solid at room temperature [2]. However, when used in conjunction with other solvents, such as DMC and DEC, thus forming a co-solvent system, the freezing point and viscosity can be lowered. Additionally, PC and EMC provide good conductivity at low temperatures and have high boiling points [2]. Most Li-ion cells employ  $\text{LiPF}_6$  as the salt because it provides high ionic conductivity and high lithium ion transfer rates, and is relatively safe [2]. Electrolyte systems based on  $\text{LiAsF}_6$ ,  $\text{LiClO}_4$ , and  $\text{LiPF}_3(\text{CF}_2\text{CF}_3)_3$  are the most widely used alternatives [2]. These systems have a higher thermal stability than  $\text{LiPF}_6$ -based electrolytes and provide long cycle life when used in combination with carbon-based anodes and metal oxide cathodes [2].

Due to the large number of possible salt-solvent combinations, a variety of different electrolytes has been used. In general, solvents must be stable at both the cathodic and anodic potentials, particularly between 0 and 4.2 V vs. Li [2]. However, none of the carbonate solvents is thermodynamically stable with lithium or  $\text{Li}_x\text{C}_6$  at 0 V vs. Li [2]. In order to account for this instability, many solvents undergo an additional reaction that forms an ion-conducting passivation film on the surface of the electrode [2]. This passivation film is referred to as the solid electrolyte interface or interphase (SEI) layer, and separates the solvent from the electrode while allowing lithium ions to pass through [2]. The formation of the SEI layer is an irreversible process that causes a relatively small loss of capacity during the cell's first cycle. The magnitude of the irreversible capacity is highly

dependent on both the type of carbon used for the anode and the electrolyte composition [2]. Because the SEI layer reaction occurs at the electrode surface, carbons with low specific area are desired [2]. The integrity of the SEI layer is critical for cell stability, performance, cycle life, and safety. The high stability of the SEI layer in EC-based electrolytes is the reason for its excellent performance and high durability [2]. Esters and alkyl carbonates, such as EC and EMC, form especially stable SEI layers that consume only a minimum amount of lithium [2].

Thin microporous polymer films, usually 10 to 30  $\mu\text{m}$  in thickness, are used as the separator to electrically isolate the anode from the cathode in Li-ion batteries [2]. Commercially available liquid-filled Li-ion cells liquid electrolytes use polyolefin separators because of their mechanical stability, chemical stability, and reasonable cost [2]. The requirements for Li-ion battery separators are high machine direction strength to allow automated winding, no shrinking or yielding in the width, resistance to puncture from electrodes, small pore size ( $< 1 \mu\text{m}$ ), high wettability by the electrolyte, and chemical compatibility with the electrodes and electrolyte [2]. Commercial microporous separators are made of polyolefins such as polyethylene, polypropylene, or laminates of both. The pore size of these separators is between 0.03  $\mu\text{m}$  and 0.1  $\mu\text{m}$  with a typical porosity of 30 to 50% [2].

### **3. Anode Materials**

Secondary lithium batteries, which employed lithium metal as the anode (negative electrode), were used before the development of today's Li-ion cells [4]. These cells had attractive performance characteristics, but were found to be unsafe. The safety issues were primarily due to the growth of lithium dendrites on the surface of the anode during cycling, which led to separator puncture and internal shorting, and the reactivity and fire hazard of the metallic lithium in general [4]. In order to overcome these challenges, researchers focused their efforts on replacing the lithium metal with a carbon-based intercalation anode, which had superior dimensional stability. Graphitic carbons were found to be

good materials for intercalation of lithium, providing a stable morphology and conserving most of the favorable performance characteristics of lithium batteries [4].

### **C. CARBON ANODES**

The first Li-ion batteries were made using petroleum coke anodes with a specific capacity of 180 mAh/g [8]. The petroleum coke showed more stability with PC based electrolytes than graphitic materials. Following petroleum coke anodes, mesocarbon microbeads (MCMB) were used as the negative electrode. MCMB consists of graphitic microspheres and show high specific capacity of up to 300 mAh/g [8]. Due to their low surface area, both the irreversible capacity (SEI layer formation) and capacity fade upon cycling are relatively low. Li-ion cells were also manufactured using low cost natural graphite as well as soft and hard carbons with good performance characteristics and energy densities of up to 700 mAh/g [8].

Today's carbon anodes can be categorized into two types, graphitic carbon and amorphous carbons, including soft and hard carbons. The type and structure of the carbon are key parameters in determining its electrochemical performance, including the lithium intercalation capacity (energy density) and the intercalation potential.

Graphitic carbon materials consists of planar sheets (graphene layers) stacked atop each other. The carbon atoms of each layer are arranged in a hexagonal lattice. There are two different types of stacking of sheets: ABABAB, also known as hexagonal graphite (2H graphite), and ABCABC, referred to as rhombohedral graphite (3R graphite) [2]. Most graphitic carbons consists of mixtures of 2H and 3R phases [2].

In amorphous carbons, stacking of layers is random and the number of well-aligned layers is small (high stacking disorder). Stacking disorder also includes rotational displacement (turbostratic disorder) and unparallel graphitic

planes (unorganized carbon) [2]. Soft and hard carbons are synthesized from organic precursor materials and are both considered amorphous carbon. Soft carbons are carbonaceous materials that contain significant amounts of hydrogen in the form of C-H bonds [7] and that can be graphitized at temperatures around 2000–3000 °C [2]. When the soft carbon is heated to high temperatures (>2000 °C), the strain in the material is relieved as the turbostratic disorder is removed. In contrast, hard carbons, typically formed from phenolic resin, cannot be graphitized. Table 5 summarized the performance characteristics of a selection of different carbon anode materials.

Carbon	Type	Specific Capacity (mAh/g)	Irreversible Specific Capacity (mAh/g)	Particle Size D <sub>50</sub> (μm)	BET Surface Area (m <sup>2</sup> /g)
KS6	Synthetic Graphite	316	60	6	22
KS15	Synthetic Graphite	350	190	15	14
KS44	Synthetic Graphite	345	45	44	10
MCMB 25–28	Graphite Sphere	305	19	26	0.86
MCMB 10–28	Graphite Sphere	290	30	10	2.64
Sterling 2700	Graphitized Carbon Black	200	152	0.075	30
XP30	Petroleum Coke	220	55	45	N/A
Repsol LQNC	Needle Coke	234	104	45	6.7
Grasker	Carbon Fiber	363	35	23	11
Sugar Carbon	Hard Carbon	575	215	N/A	40

Table 5. Properties and performance of various carbons. An ideal carbon material would offer high specific capacity without irreversible capacity (From [2]).

## 1. Graphite

Graphite is the most widely used anode material in Li-ion batteries. It has a theoretical specific capacity of 372 mAh/g ( $\text{LiC}_6$ ) and exhibits good cycling performance and very little irreversible capacity [10]. The voltage profile during the charge and discharge process in graphite is shown in Figure 5 (plot A) and does not exhibit significant hysteresis [7]. As lithium is intercalated into the graphite the ABAB stacking turns into AAAA stacking denoted by pronounced plateaus in the voltage profile (not shown). The lithium forms islands within the graphite instead of spreading homogeneously. The most lithium rich stage,  $\text{LiC}_6$ , is formed at the lowest voltage ( $\sim 0.1$  V vs. Li) [2].

Several intercalation/deintercalation studies were conducted on natural graphite [7]. Although the studies were brief and introductory, the slow-scan cyclic voltammograms revealed that the intercalation and deintercalation processes occur within a range of 300 mV versus  $\text{Li/Li}^+$  [7]. This directly correlates to the great discharge potential values that characterize graphite-based Li-ion batteries. It was also discovered that the allotropic modifications have an effect on the performance of graphitic anodes. The rhombohedral form is stable at lower temperature and thus, exhibits better cycle-life and structural stability [7].

Propylene carbonate (PC) decomposition at graphitic anodes during charging is quite severe. The reason is the co-intercalation of solvated  $\text{Li}^+$  ions, which results in exfoliation and damage of the lattice structure. Eventually, it was discovered that use of ethylene carbonate (EC) inhibits co-intercalation, leading to the replacement of PC with EC in Li-ion battery electrolytes [2]. Mesocarbon microbeads and graphite fibers were one of the successful performing modified graphite materials as it was able to intercalate/de-intercalate Li ions over long distances across the graphene layers [8]. In addition, ball-milling of the mesocarbon microbeads have been conducted to change the particle size and

study the effects on the performance of Li-ion batteries. Researchers are looking into other modified graphitic anode materials to investigate their suitability for Li-ion batteries [7].

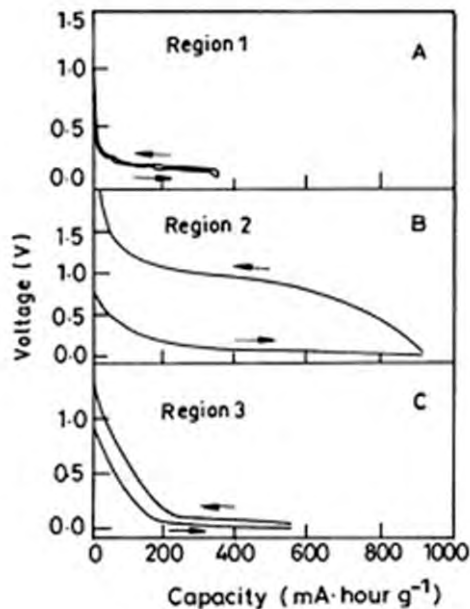


Figure 5. Voltage vs. capacity plot (second cycle) of three different carbon anodes: synthetic graphite (region A), soft carbon derived from petroleum pitch at 500 °C (region B), and hard carbon from resole resin heat-treated at 1000 °C (region C). Lithium metal is used as reference and counter electrode (From [7]).

## 2. Soft Carbons

Soft carbons can store large quantities of lithium and thus exhibit high specific capacity (up to 700 mAh/g).[6] Note that you have to multiply specific capacity by voltage to obtain the units of energy; mAh/g has the units of specific capacity. One of the major disadvantages of soft carbons is the high overvoltage during discharge (overall voltage loss). Unlike graphite, disordered carbons have continuous sloping voltage profiles with an average discharge voltage of ~0.3 V (vs. Li), and do not show distinct lithiation/delithiation voltage plateaus [2].

The specific capacity of soft carbons decreases to ~180 mAh/g when increasing the heat treatment temperature to about 1700°C [7]. Because of the large amount of hydrogen in the form of C-H bonding, large quantities of lithium ions can be stored which leads to high capacity [7].

Additionally, a hysteresis exists in the voltage profile at about 0.0 V [6]. The hysteresis is due to the irreversible capacity resulting from the SEI layer formation and side reactions occurring within the cell. Because of the considerable overvoltage during discharge, soft carbons are considered unsuitable for Li-ion batteries [7].

### **3. Hard Carbons**

Hard carbons are synthesized by heat treatment of organic precursors in the temperature range of 800–1200°C [7]. In contrast to soft carbons, hard carbons contain significantly less hydrogen and therefore, less C-H bonding [7]. Hard carbons are non-graphitized carbon platelets and are generally disordered. [7] Hard carbons heated at 1100 °C exhibit a reversible capacity of 600 mAh/g, but are also subject to irreversible capacity losses and hysteresis between charge and discharge (Figure 5, plot C) [8].

The specific capacity of hard carbons tends to decrease with heat treatment temperature, reaching a minimum of ~180 mAh/g at 2000°C [7]. Spherical hard carbon materials were found to exhibit the best electrochemical performance; however, spherical hard carbons are difficult to synthesize. Most commercially available hard carbon anodes show a capacity between 200 and 600 mAh/g over a voltage range of 0–1.5 V vs. Li/Li<sup>+</sup> [9]. The disadvantages of hard carbon materials include low initial coulombic efficiency due to large irreversible capacity, low tap density and poor electrical conductivity [9].

The suitability of a particular carbon material is determined by its chemical stability, charge-discharge cycling efficiency, and the total reversible charge capacity (energy density) [7]. Figure 6 shows the reversible charge capacity

(energy density) of various hard and soft carbons as a function of their crystallite size (stacking thickness). While composition and microstructure of these carbons vary substantially, that there exists a clear dependence on the level of graphitization. For crystal sizes  $>10\text{nm}$ , the Li-ion storage process followed the known mechanism of ion intercalation in layered graphite [8]. However, the large increase in capacity for small crystal sizes ( $<2\text{ nm}$ ) cannot be explained with the traditional point of view.

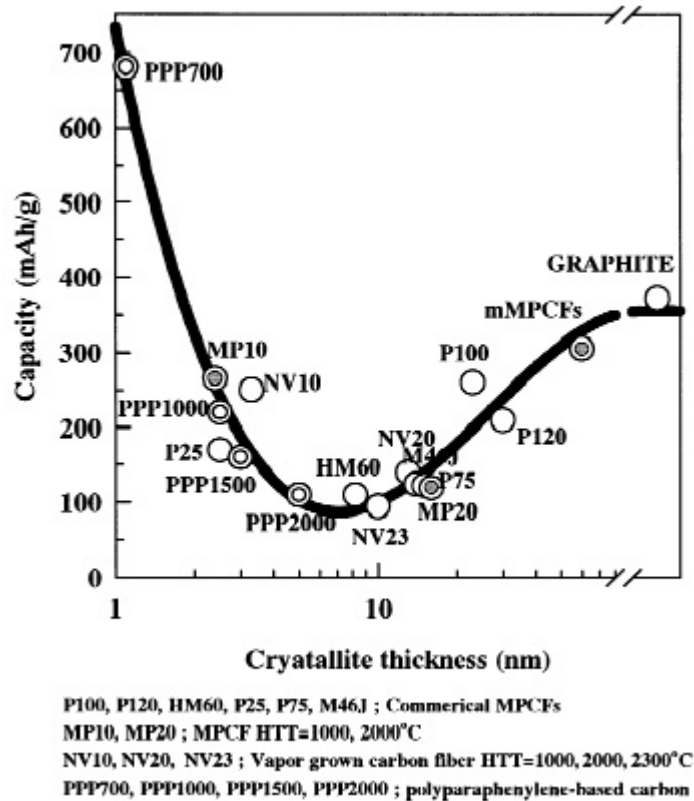


Figure 6. Specific charge capacity of the various kinds of carbon fiber and PPP-based carbon electrodes at the second cycle as a function of crystallite thickness,  $L_{c(002)}$ , determined by X-ray diffraction analysis. Dahn et al. also proposed three regions of lithium insertion capacity by the heat treatment temperatures of carbon materials (From [8]).

Although progress has been made in developing carbon-based Li-ion battery anodes with higher energy density and improved power characteristics,

the charge storage mechanism in these disordered carbons is not well understood [8]. A better understanding of the lithiation/delithiation processes in amorphous carbons may allow for a reduction of the irreversibility capacity and the charge overvoltage, while maximizing the reversible capacity. Once the governing structure-performance relationship has been identified, low cost carbons with tailored properties and superior performance can be designed.

#### **4. Carbide-Derived Carbon**

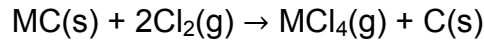
Nanoporous carbide-derived carbon (CDC) is a relatively new type carbon material that is synthesized with/through high-temperature chlorination (halogenation) of metal carbides [10]. Structurally, CDCs encompass a large range from very disordered (amorphous carbon) to highly ordered material (graphitic carbon) and even carbon nanotubes and graphene [10]. The final CDC structure is highly dependent on the process parameters, such as chlorination temperature, pressure, and choice of carbide precursor [10]. The most attractive feature of CDCs is the ability to control and adjust their structural features, such surface area, degree of graphitization, crystal size, and porosity, in a precise and homogenous fashion [10]. This makes CDC an ideal candidate material to study the effect of structural features on the Li-ion storage capacity in amorphous carbons.

#### **5. Synthesis**

Halogenation of metal carbide via chlorination is the most popular method to synthesize CDC. It allows for selective extraction of metal atoms from the carbide lattice at temperatures as low as 200°C and ambient pressure for most carbide [12]. In addition, chlorination is the most economic and scalable method. CDC can also be produced by acid etching, hydrothermal treatment, and vacuum decomposition [13].

Most chlorination processes run at temperatures between 200 and 1200°C (Figure 7). The metal atoms are etched away by the chlorine gas, leaving behind

a highly amorphous carbon (Figure 7a). During chlorination, the carbon phase is produced by inward growth while retaining shape and volume of the original precursor [13]. CDCs have successfully been derived from various precursors, including SiC, TiC, Ti<sub>3</sub>SiC<sub>2</sub>, VC and Mo<sub>2</sub>C (see Table 6) [12]. The halogenation reaction for binary carbides is:



Note in this general halogenation reaction for binary carbides, “M” denotes the precursor material (e.g., M = Si, Ti, Zr) [12].

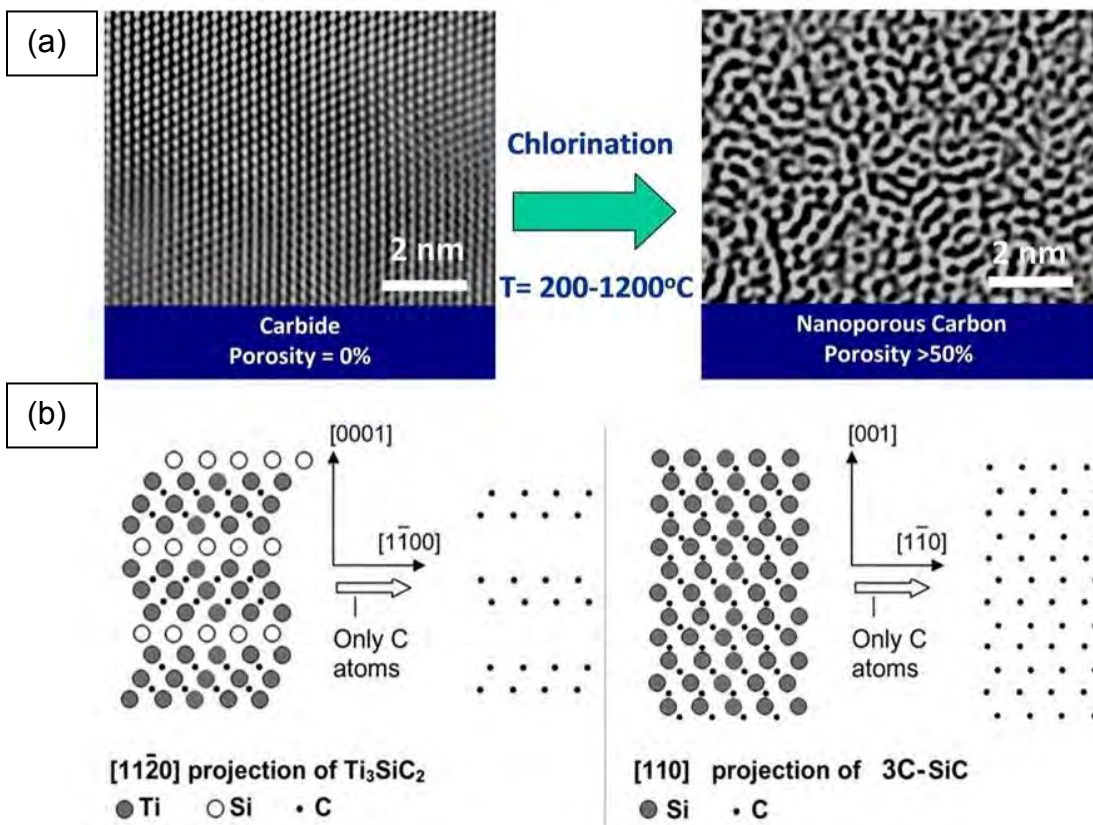


Figure 7. (a) High-resolution transmission electron microscopy (HRTEM) image of metal carbide before and after chlorination. (b) Schematic illustrating the importance of precursor material on final CDC structure (From [11]).

Structure and porosity of the synthesized carbon depend strongly on the composition of the precursor carbide, as illustrated in Figure 7b [11]. Key

advantages of CDCs over other kinds of porous carbon materials include a very narrow, adjustable pore size distribution and an exceptionally high surface area [11].

SiC	Silicon Carbide	Nb <sub>2</sub> C	Niobium Carbide
TiC	Titanium Carbide	NbC	Niobium Carbide
Mo <sub>2</sub> C	Molybdenum Carbide	SrC <sub>2</sub>	Strontium Carbide
VC	Vanadium Carbide	Ta <sub>2</sub> C	Tantalum Carbide
Al <sub>4</sub> C <sub>3</sub>	Aluminum Carbide	TaC	Tantalum Carbide
B <sub>4</sub> C	Boron Carbide	Ti <sub>2</sub> AlC	Titanium Aluminum Carbide
BaC <sub>2</sub>	Barium Carbide	Ti <sub>3</sub> AlC <sub>2</sub>	Titanium Aluminum Carbide
CaC <sub>2</sub>	Calcium Carbide	Ti <sub>3</sub> SiC <sub>2</sub>	Titanium Silicon Carbide
Cr <sub>3</sub> C <sub>2</sub>	Chromium Carbide	W <sub>2</sub> C	Tungsten Carbide
Fe <sub>3</sub> C	Iron Carbide	ZrC	Zirconium Carbide
MoC	Molybdenum Carbide		

Table 6. Carbide-derived carbon precursors for synthesizing CDC materials (From [12]).

## 6. Structure and Properties

Pore size, pore size distribution, and specific surface area of CDCs depend on the carbide precursor as well as the chlorination temperatures. Below 600°C, there exists no crystallinity and the CDC is highly amorphous [12]. At temperatures below 1000°C, structural ordering increases with increasing chlorination temperature, but stacking of well-aligned, parallel graphene layers is not observed [12]. At higher chlorination temperatures (>1000°C) graphitic phases dominate, and graphite ribbons and nanocrystalline graphite (3–4 layers) are formed [12]. Therefore, the general trend in structural development of CDCs is synthesis of amorphous and highly disordered carbon at low temperatures, and increasingly crystalline carbon with graphitic ribbons at higher chlorination temperatures [12].

Figure 8 shows the X-ray diffraction pattern of TiC-CDC chlorinated at different temperatures between 200 and 1200°C. The complete conversion of TiC to carbon occurs at temperatures as low as 400°C, as indicated by

disappearance of the TiC diffraction peaks between 300 and 400°C [10]. The lack of a sharp XRD feature around 26°, observed for graphitic carbons, suggests the presence of highly amorphous sp<sup>2</sup> carbon without significant layer stacking.

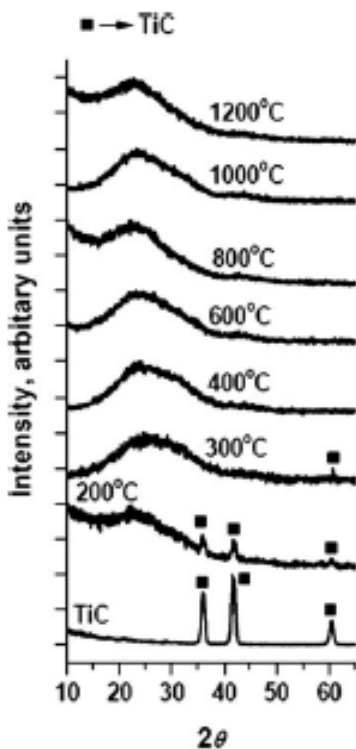


Figure 8. XRD of TiC and TiC-CDC samples synthesized at different temperatures. Complete conversion of TiC to carbon takes place at 400°C and above. Broad peaks show the highly amorphous nature of the carbon produced from TiC (From [10]).

## 7. Application in Energy Storage

Applications for CDCs in energy storage range from catalyst support in fuel cells to electrodes for supercapacitors and Li-ion batteries, and storage media for hydrogen and methane gas [10].

CDCs tunable structure and porosity, synthesized from TiC, SiC, Ti<sub>2</sub>AlC, B<sub>4</sub>C, Al<sub>4</sub>C<sub>3</sub>, Mo<sub>2</sub>C, and VC, have been investigated as potential electrode

material for supercapacitors [12]. The differences in pore volume and pore size distribution as well as the carbon structure from the various ceramic precursors were found to strongly affect the capacitance of the resulting CDC [12]. The parameter with the greatest impact on the capacitance of the CDC was found to be the synthesis temperature [12]. The tunability of CDC pore size led to a breakthrough in understanding the capacitive charge storage mechanism in porous carbons. With the ability to tune the pore size and control the pore size distribution, optimization of CDC electrodes is easier for a variety of different electrolytes than other types of carbon material.

The use of CDC as electrode materials for Li-ion batteries remains largely unexplored. While few studies of SiC-, TiC-, and Mo<sub>2</sub>C-derived CDCs investigated the composition of the CDC upon charge and revealed the presence of LiC<sub>12</sub>, LiC<sub>24</sub>, LiC<sub>6</sub>, Li<sub>2</sub>CO<sub>3</sub>, and Li<sub>2</sub>C<sub>2</sub> phases, no data on energy density, power density, and cycle life was presented [12]. While lithium ion (Li<sup>+</sup>) diffusion is expected to occur mainly along the pore walls and Li is believed to accumulate in the pores forming metal clusters, no comprehensive model and no conclusive experimental evidence exists that support these claims [12]. Disordered carbons and CDC in particular may offer faster charge/discharge rates and longer cycle life compared to graphitic electrodes. However, further research is needed to investigate the charge storage mechanism in CDC and determine the key parameter that governs its electrochemical performance in Li-ion batteries.

#### **D. THESIS OBJECTIVES**

The objective of this study is to fabricate, characterize, and test CDC-based battery electrodes and to explore their potential for Li-ion battery applications. In particular, the following tasks will be performed:

- Develop and optimize a process that allows us to fabricate fully functionally Li-ion battery electrodes using commercially available anode and cathode powders.

- Using the developed processes, fabricate CDC anodes with three different types of TiC-CDC synthesizes at 600, 1000 and 1200°C.
- Characterize the battery materials and the custom-build electrodes using X-ray diffraction (XRD), scanning electron microscopy (SEM), and Raman spectroscopy.
- Assemble the fabricated electrodes into operational button-type coin cell batteries and analyze their electrochemical performance.

THIS PAGE INTENTIONALLY LEFT BLANK

## II. EXPERIMENTAL SECTION

### A. MATERIALS

Building a functioning Li-ion battery requires a variety of different materials. Li-ion batteries are typically comprised of an anode, cathode, binder, current collector, separator, electrolyte, solvent, and the battery casing. While there are many variations of battery sizes and shapes, in this study we utilized button-type coin cell cases. All battery materials were obtained from MTI Corporation, unless indicated otherwise.

Three different anode materials were used in this study. The first anode material was a commercially available graphite anode (specific capacity: 330 mAh/g, active material density: 120 g/m<sup>2</sup>). The second anode material was metallic lithium, also obtained from MTI Corporation (thickness: 0.15 mm, specific capacity: 3,862 mAh/g). The third anode material used in this study was CDC. Three different types of CDC, synthesized (chlorinated) from TiC at 600, 1000, and 1200°C, were used and provided in powder form by Y-Carbon, Inc. The cathodes used were either commercial lithium cobalt oxide (LiCoO<sub>2</sub>) anodes or lithium (Li) metal.

Polyvinylidene fluoride (PVDF) was used as polymer binder for fabricating the electrodes from CDC powders. The solvent used for the PVDF binder was N-Methyl-2-Pyrrolidone (NMP, C<sub>5</sub>H<sub>9</sub>NO). Current collectors were aluminum foil (Reynolds) for the cathode and copper foil for the anode. Microporous polyolefin (thickness ~0.1 μm) served as separator material. The electrolyte was composed of 1 M LiPF<sub>6</sub> and a mixture (1:1:1) of ethylene carbonate (EC), dimethyl carbonate (DMC), and ethyl methyl carbonate (EMC).

The CR2032 coin cell casings (stainless steel) consisted of four components: top case (cathode side), bottom case (anode side), spacer (15.4 mm X 1.1 mm), and spring (15.8 mm X 0.5 mm).

## **B. CHARACTERIZATION METHODS**

Several different characterization techniques were used to analyze the structure and electrochemical performance of the anode and cathode materials, including X-Ray Diffraction (XRD), Raman Spectroscopy and Scanning Electron Microscopy (SEM).

### **1. X-Ray Diffraction**

The signal measured during XRD consists of high-energy electromagnetic radiation with energies ranging from 200 eV to 1 MeV. The X-rays are created in an X-ray tube, which contains two metal electrodes in a vacuum chamber. The electrons are emitted from a heated tungsten filament (cathode) and accelerated toward the anode at ground potential. The high velocity electrons collide with the anode (chilled by water) and emit X-rays upon collision with the anode. Only 1% of the entire electron beam is converted to X-rays while the remaining majority is dissipated as heat in the chilled anode. If the colliding electron has enough energy to eject an inner-shell electron from the atoms in the anode, an X-ray photon, created from the replacement of the ejected electron by an outer shells electron, is emitted. The energy of the X-ray photon is a fingerprint of the anode material. This characteristic, monochromatic radiation is used for the diffraction measurements.

The diffraction results from the constructive interference of the X-rays that are scattered by the atoms from a set of crystal planes within the specimen. An X-ray diffractometer consists of three primary components, the X-ray source, the X-ray detector, and the specimen holder. The goniometer, which holds the material specimen, is the central part of the X-ray diffractometer. Both X-ray detector and X-ray source are mounted on side arms. The Bragg angle, theta ( $\theta$ ), is the angle between the plane of the specimen and the X-ray source. The angle between the X-ray detector and the projection of the X-ray source is referred to as  $2\theta$ . During operation the X-ray source is fixed while the X-ray detector moves

through the range of angles ( $0^\circ < 2\theta < 170^\circ$ ) and collects the XRD pattern. The Phillips MRD X-Ray Diffractometer uses the Cu  $K_\alpha$  line as radiation source (8.04 keV energy, 0.1542 nm wavelength) [14]. During XRD analysis, the diffractometer was operated at a voltage of 35 kV and current of 30 mA.

In order to characterize the CDC powders, a thin film of silicon grease was spread onto a glass microscope slide. A thin layer of CDC powder was then sprinkled on top of the silicon grease. The silicon grease was required to ensure that the powders adhered to the glass substrate during measurements.

## **2. Scanning Electron Microscopy**

Scanning electron microscopy (SEM) is a very powerful characterization technique, capable of imaging materials and surfaces at the nanometer scale. In contrast to light microscopy, which images samples through the reflected light, SEM uses electrons to visualize the material structure and is not limited by the diffraction limit of visible light. The maximum magnification of light microscopy is approximately 2,000X [15]. In contrast, electrons have a wavelength of 0.5 Å with a theoretical maximum magnification of greater than 800,000X [15]. However, for practicality the SEM limits for magnification are ~75,000X or 40 Å. SEM microscopes are operated under high vacuum conditions ( $\geq 10^{-4}$  torr) [15]. The high vacuum is necessary to prevent scattering of the electron beam by residual gas molecules and to inhibit oxidation of the cathode filament.

The accelerating voltage of the electrons ranges from 1 to 30 keV [15]. The voltage used depends on the type of material analyzed. The diameter of the electron beam is one of the most crucial parameters in SEM imaging as it determines the spatial resolution. Typical beam diameter range from 100 to 200 Å. For high resolution imaging beam sizes of ~50 Å or lower are required [15].

Another crucial parameter for obtaining high quality SEM images is the scan speed. The scan speed, which can be set between 100 and 100,000 lines/scan, is simply the rate at which the electron beam passes over the sample

[15]. Faster scan rates create a static, low quality image used to explore the sample and locate areas of interest. Slower scan rates allow for more detailed, high quality images and are used for collecting the SEM image from the area of interest.

There exist two different types of signals that can be obtained from the electron bombardment, depending on the nature of the electron-specimen interaction. The scattering events are either elastic (electron-nucleus interaction) or inelastic (electron-electron interaction) collisions of beam (primary) electrons with the specimen atoms [15]. Elastic collisions create backscattered electrons (BSE), which give compositional and topographic information about the sample material. In contrast, inelastic collisions deposit energy within the sample by exciting specimen atoms. The excited atoms then return to the ground state by releasing energy in the form of secondary electrons (SE), X-rays, light photons, and phonons [15].

The atomic weight ( $Z$ ) of the specimen also affects SEM imaging. A higher  $Z$  of the specimen will ensure a higher probability of backscattering than a specimen of a lower  $Z$  [15]. Therefore, backscattered imaging allows for distinguishing spots of different  $Z$  within a sample.

SEM images were recorded using a Zeiss Neon 40 field emission SEM with focused ion beam. The microscope has 0.9 nm resolution at 20kV and is equipped with an Energy Dispersive Analysis of X-Rays (EDAX) and a backscattered electron (BSE) detector. For SEM analysis, the TiC-CDC 600 and 1000°C anodes were mounted on a conductive substrate with carbon tape and then secured to the xyz sample stage of the SEM.

### **3. Raman Spectroscopy**

Raman spectroscopy utilizes the Raman Effect to characterize structure and composition of materials. The Raman Effect, which describes the change in

the wavelength of light that occurs when a light beam is deflected by molecules and crystalline solids, is named after Sir C.V. Raman who received the Nobel Prize in 1930 for his discovery [16].

When the incident photons collide with the atoms of the specimen, a large fraction of the photons are scattered elastically, and do not change their energy upon collision. This scattering is known as Rayleigh scattering [16]. However, a small fraction of the incident photons experiences a change in energy as a result of an inelastic scattering event (Raman scattering). In Raman scattering, the atoms in the crystal lattices gain or lose energy [16]. Stokes Raman scattering refers to an increase in energy. The photon excites the specimen atoms to a higher vibrational or rotational energy state, and therefore loses energy upon scattering [16]. If the specimen atoms are already in an excited vibrational state, the photon gains energy from the collision [16]. This effect is known as Anti-Stokes Raman scattering [16]. At room temperature, Stokes Raman scattering is more likely to occur since most molecules are at a ground state. Therefore Stokes scattering gives the stronger Raman signal and is generally used for Raman analysis.

The Raman frequency, or Raman shift, is the difference (in wavenumbers) between the frequency of the incident light and the frequency of the scattered light [16]. The Raman shift is thus a direct measure of the vibrational energies of a material and correspond to vibrational or rotational transitions of the scattering atoms [16].

Raman spectra were collected under 514 nm (Ar ion) laser excitation using an inVia Confocal Raman Microspectrometer (Renishaw Inc.) with Raman imaging and Raman mapping capabilities. Measurements were taken in backscattering geometry using a 50x objective, a 1800 l/mm grating, and a 50  $\text{cm}^{-1}$  cut-off notch filter. Typical measurement times were between 2 to 3 minutes (5 accumulations, each at ~30 s).

### **C. MACCOR BATTERY TESTER**

The button-type coin cells that were constructed were tested and cycled. The Maccor 4200 Battery Tester used for cycling had 16 channels that were capable of delivering a voltage of  $\pm 5$  V or 0 to 10 V, a current of 150  $\mu$ A to 15 A, and charge and discharge powers of 2400 Watts.

### III. RESULTS AND DISCUSSION

The development of a new Li-ion battery material consists of multiple sequential steps, including material synthesis and characterization, electrode fabrication, battery assembly, and battery testing. Electrode fabrication is one of the most crucial steps in battery development. This process determines the final energy and power characteristics of the battery. Therefore, before analyzing the electrochemical performance of a new anode material, one has to develop proper electrode fabrication methods and optimize the individual process steps.

#### A. ELECTRODE PRODUCTION

Both anode and cathode electrodes were made from their respective powders. Anode materials included graphite and CDC (chlorinated at 600°C, 1000°C, and 1200°C). Cathode powders used were  $\text{LiCoO}_2$ ,  $\text{Li}(\text{Ni},\text{Mn},\text{Co})\text{O}_2$  (1:1:1),  $\text{Li}(\text{Ni},\text{Mn},\text{Co})\text{O}_2$  (5:3:2), and  $\text{LiFePO}_4$ . While the procedures for the different powders were the same, the specific amounts of each component, including polymer binder and conducting carbon additive varied. The development of the required fabrication steps and establishment of proper electrode recipes for battery research at NPS were among the primary objectives of this thesis.

##### 1. Electrode Powder Preparation

The as-received anode and cathode powders were mixed PVDF binder and acetylene black. The PVDF binds the powder particles together and enables the powder to adhere to the current collector foil (copper or aluminum). Acetylene black, which is a form of active carbon, is used to increase the electronic conductivity of the electrode. Graphite,  $\text{LiCoO}_2$ ,  $\text{LiFePO}_4$ ,  $\text{Li}(\text{Ni},\text{Mn},\text{Co})\text{O}_2$  (5:3:2) and  $\text{Li}(\text{Ni},\text{Mn},\text{Co})\text{O}_2$  (1:1:1) powders were mixed with 10 wt% of acetylene black

and 10 wt% of PVDF. CDC powders exhibit sufficient electronic conductivity and were mixed with 15 wt% PVDF. Figure 9 shows the powder composition of a  $\text{LiFePO}_4$  cathode.

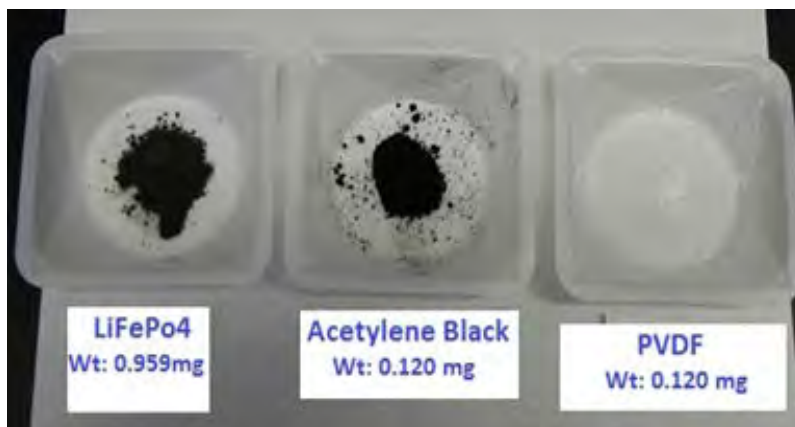


Figure 9.  $\text{LiFePO}_4$ , acetylene black, and PVDF powders in weighing boat before mixing.

After the different components were added, the powder mixtures were ball-milled for 30 min using a 8000 M SPEX Sample Prep Mixer/Mill (Figure 10).



Figure 10. The 8000 M SPEX Sample Prep Mixer/Mill used to ball mill anode or cathode powders together with acetylene black and PVDF binder.

The ball milling reduces the agglomerate size and thoroughly mixes the powders to ensure a uniform composition.

## 2. Slurry Preparation and Electrode Casting

After ball milling, powders were weighed and added to a glass vial. NMP solvent was added to dissolve the PVDF and prepare a slurry suitable for electrode casting. Due to the volatile and hazardous nature of the solvent, this step was done under a fume hood using a glass pipette and a pipette dispenser (Figure 11a).



Figure 11. a) Slurry preparation setup under the fume hood with NMP solvent, glass pipette with dispenser, and the ball milled powder mixture containing  $\text{LiFePO}_4$ , acetylene black, and PVDF binder; and b) Prepared slurry after adding NMP solvent to the powder mixture.

The procedures for making the slurries were the same for all electrodes. The differences are in the powder-to-solvent ratio due to differences in material density and dispersion. The optimized recipes for the various electrodes are summarized in Table 7.

Active Material		Additives			Applicator Height (mm)
Type	Weight (g)	PVDF (g)	Acetylene Black (g)	NMP (mL)	
<b>Anode</b>					
Graphite	1	0.1	0.1	4.5	4
CDC 600 °C	0.51	0.09	0	3.5	4
CDC 1000 °C	0.51	0.09	0	3.5	4
CDC 1200 °C	0.51	0.09	0	6.5	4
<b>Cathode</b>					
LiCoO <sub>2</sub>	1	0.1	0.1	3.4	4
LiFePO <sub>4</sub>	1	0.1	0.1	3.4	
Li(NiMnCo)O <sub>2</sub> (5:3:2)	1	0.1	0.1	3.6	4.5
Li(NiMnCo)O <sub>2</sub> (1:1:1)	1	0.1	0.1	3.4	4

Table 7. Optimized recipes of different electrode mixtures listing the amounts of active material, acetylene black, PVDF binder and NMP solvent.

After the slurry was prepared, the cap of the vial was secured with paraffin wax paper to ensure proper enclosure of the volatile solvent.

The vial with the electrode slurry was then placed in an ultrasonic bath (PC3 Ultrasonic Cleaner) for a total of 30 min to dissolve the PVDF (Figure 12). The slurry was stirred every ten minutes to ensure proper mixing.



Figure 12. Sample vial containing a  $\text{LiFePO}_4$  slurry inside the ultrasonic bath. Each vial was sonicated for 30 minutes.

While the electrode vial was inside the ultrasonic bath, the current collector foil was prepared. Aluminum foil was used for cathodes and copper foil was used for anodes. The current collector foil was cut into squares (4'x4') and flattened onto the glass plate using ethanol and Kim wipes. The foil was then taped to the glass plate, as shown in Figure 13, and placed under the fume hood.

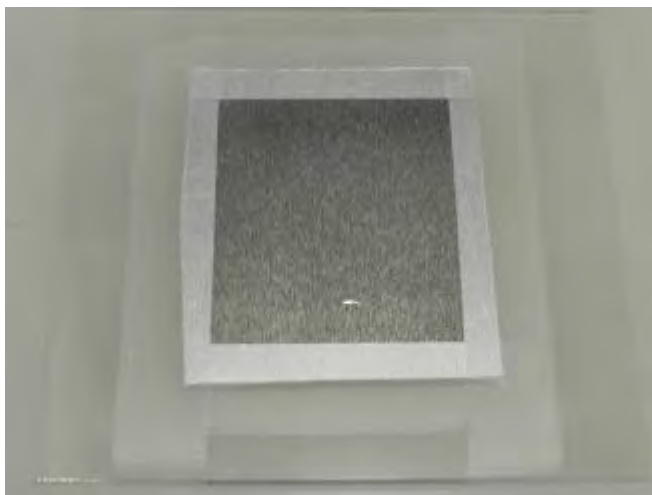


Figure 13. Aluminum foil current collector taped on a glass plate. The foil was flattened with Kim wipes and ethanol.

A micrometer adjustable film applicator was used to cast the electrode slurry on top of the current collector under the fume hood. The applicator allows us to control the thickness of the electrode film by adjusting the micrometer screws on top. Before casting, the electrode slurry was mixed for about 2 min to ensure high homogeneity.

After extensive stirring, the slurry was poured onto the current collector foil (Figure 14a). Subsequently, the glass slide was pushed back and forth underneath the applicator blade to distribute the slurry on top of the foil with a constant thickness (Figure 14b).

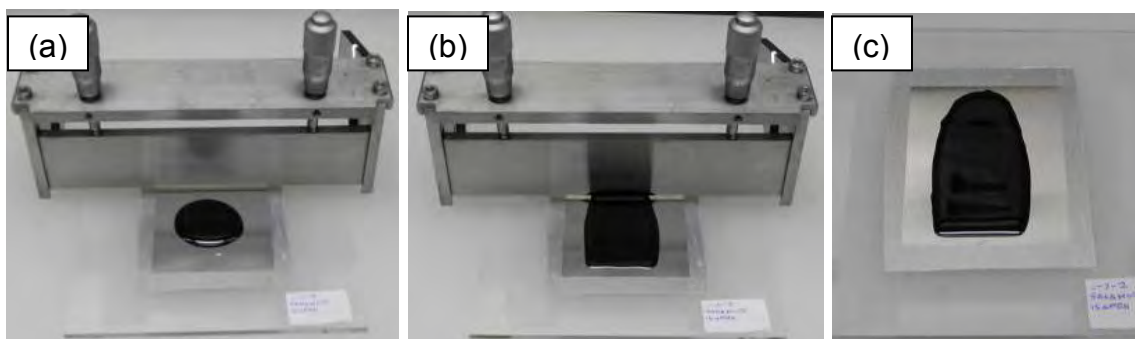


Figure 14. (a)  $\text{LiFePO}_4$  slurry laid onto foil current collector and (b)  $\text{LiFePO}_4$  slurry casted with applicator and (c)  $\text{LiFePO}_4$  casted.

Care was taken to prevent the slurry from touching the tape as the containing solvent can dissolve the tape and contaminate the electrode. Figure 14c shows a  $\text{LiFePO}_4$  cathode after casting. The wet electrodes were placed in a drying oven and dried overnight at  $100^\circ\text{C}$ . The drying step in the oven was found to be necessary to prevent the electrodes from cracking. Electrodes dried at ambient temperature under the fume hood showed extensive cracking and flake formation. Further investigation revealed that both the air flow in the fume hood and insufficient PVDF caused the electrodes to crack and flake. Figure 15a and 15b show two  $\text{LiFePO}_4$  cathodes of the same composition dried under the fume hood and in the drying oven, respectively. Figure 15c shows an example of a TiC CDC  $600^\circ\text{C}$  anode.

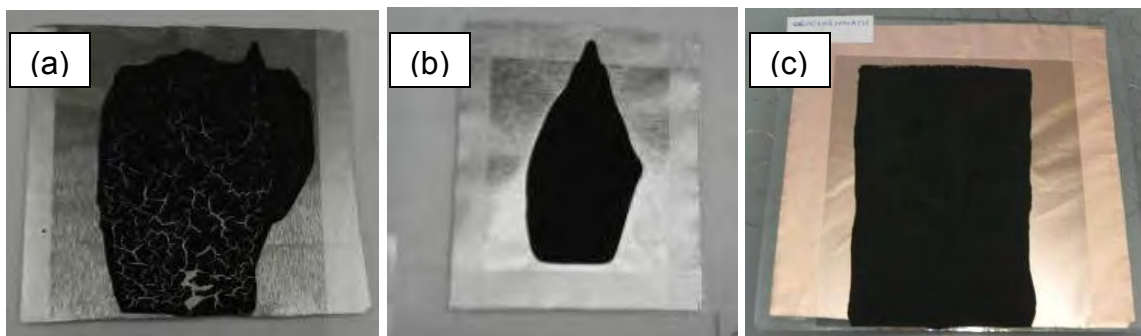


Figure 15. (a)  $\text{LiFePO}_4$  dried film with cracks and flakes and (b)  $\text{LiFePO}_4$  dried film and (c) TiC CDC 600 °C film.

Once the films have dried, the electrodes were removed from the glass slide and cut to 12 mm-diameter disk electrodes using a hole puncher (Figure 16).

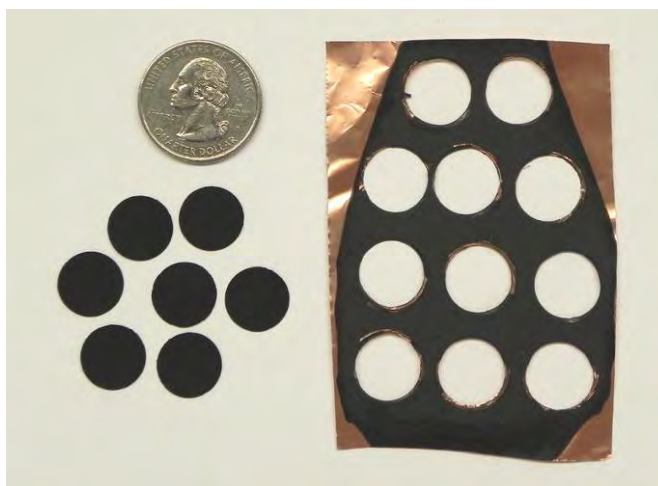


Figure 16. Disk-shaped TiC CDC 600°C coin-cell anodes were punched out from dried electrode films.

After the electrodes were punched out, they were weighed and labeled according to their type and the location on the current collector foil. Measuring the weight of each individual disk electrodes allowed us to determine the homogeneity of the films. It was discovered that the distribution of active material

was not consistent. The weights of the electrodes at the edges of the film were less than the weight of the electrodes in the middle, probably due to a slightly uneven surface during casting.

The disk electrodes were put on a glass slide and placed overnight in a drying oven to remove the moisture from the electrodes. After drying, electrodes were transferred to the side chamber of an argon-filled glove box (Figure 17) in which the button-type coin cell batteries were fabricated.



Figure 17. An Argon-filled glove box was used to prepare and assemble the coin cell batteries. The glove box prevents the electrodes from getting in contact with oxygen and moisture, both of which are known to reduce the cycle-life of Li-ion batteries.

Once the chamber of the glove box was secured, it was evacuated and put under vacuum (-30 psi) for 5 min and 30 min for the small and large transfer chamber, respectively. After evacuation time has elapsed, the chamber was brought back to atmospheric pressure using the argon from inside the glove box. The electrodes were then transferred to the inside the glove box where the batteries were assembled. Li-ion battery electrodes and must be handled in an inert atmosphere to ensure that no moisture or other contaminants get in contact with battery parts prior to the assembly.

Once the electrodes were inside the glove box, construction of the button-type coin cells began. The negative side of the coin cell was placed at the bottom, followed by the spring and three spacers, which ensured that the electrodes were not lose or moving freely within the case.



Figure 18. Button-type coin cell assembly schematic.

The anode was placed on top of the spacers, with the active material facing up, and soaked in 4–5 drops of electrolyte. The separator was then placed on top of the anode and soaked with 4–5 drops of electrolyte. In a third step, the cathode, with the active material facing down, was put on top of the separator. Finally, the top part of the button-type coin cell case was put atop the assembly, and pushed down slightly to close the casing. After assembly, coin cell were fully closed and sealed by an automatic coin cell-crimping machine. Following the crimping process, the open circuit potential (voltage) of each coin cell was measured and recorded. Nonfunctional cells were marked and removed from the glove box together with the operational batteries. Functional coin cells were labeled and properly catalogued before testing.

## B. ELECTRODE CHARACTERIZATION

In order to relate the electrochemical performance of carbon to its structural features, one must properly characterize the electrode materials prior to battery assembly and testing. Key parameters believed to determine the electrochemical performance of carbon anodes in Li-ion batteries are: (1) Formation and ordering of monoatomic graphite layers (graphene), (2) layer stacking, and (3) microstructural features, such particle size and porosity. In this study, Raman spectroscopy and X-ray diffraction were used to study the in-plane and stacking order, respectively. The microstructure of the carbon anodes was analyzed by scanning electron microscopy (SEM).

### 1. X-Ray Diffraction Results

The X-ray diffraction pattern of TiC-CDC synthesized at 600, 1000, and 1200°C is shown in Figure 19. The background features from the sample holder and the XRD pattern of nanocrystalline graphite are displayed for comparison.

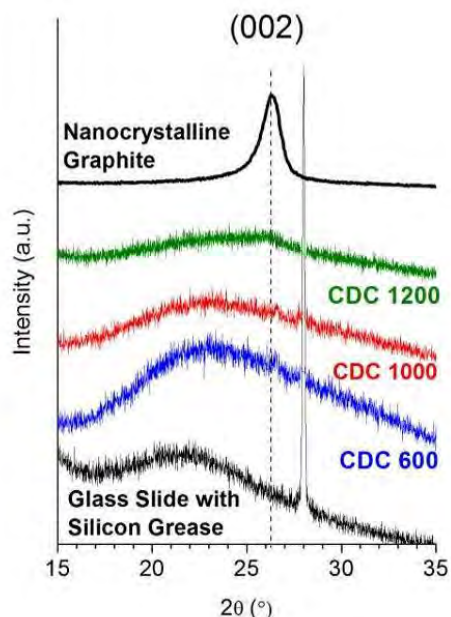


Figure 19. X-ray diffraction pattern of TiC-CDC synthesized 600, 1000, 1200°C, in comparison to data collected from nanocrystalline graphite.

Figure 19 suggests that all three TiC-CDC samples are highly amorphous, as indicated by the absence of the (002) scattering feature around  $2\Theta = 26^\circ$  resulting from the layer stacking in graphitic materials (see XRD pattern of nanocrystalline graphite). The broad peak between  $15$  and  $30^\circ$  is characteristic for highly amorphous materials that lack any long-range order and do not exhibit sharp diffraction peaks as seen in crystalline specimens. Peak broadening is caused by a reduction of the crystal size and increasing disorder. As ordering increases at higher synthesis temperatures, the intensity of the broad peak decreases. However, even CDC synthesized at  $1200^\circ\text{C}$ , does not show any sharp graphitic scattering peaks.

## 2. Raman Spectroscopy

A small amount of each TiC-CDC powder was placed on top of silicon (Si) wafer. Using a substrate material with characteristic Raman spectrum, such as Si, allows us to account for any possible contributions from the substrate material.

The powder samples were flattened with a spatula to create a smooth surface for Raman analysis. Raman spectra from different sample areas were recorded in order to determine the homogeneity of the CDC powders.

The Raman spectra recorded from TiC-CDC  $600^\circ\text{C}$  are displayed in Figure 20. Like most carbon materials, CDC exhibits two first-order Raman peaks, referred to as D band ( $\sim 1350\text{ cm}^{-1}$ ) and G band ( $\sim 1580\text{ cm}^{-1}$ ) [10]. The D-band is linked to disorder and lattice defects within the material, whereas the G-band corresponds to the in-plane vibrations of the  $\text{sp}^2$ -bonded carbon atoms and represents the level of graphitic ordering [10]. The intensity ratio between the D and G bands (D/G) is often used as a measure of graphitic ( $\text{sp}^2$ ) ordering, or graphitization, of carbon samples [10]. However, it should be noted that “graphitic ordering” refers to the ordering of the  $\text{sp}^2$  bonding, not to layer stacking as in XRD. Spectra were normalized with respect to the maximum intensity, which is the G band.

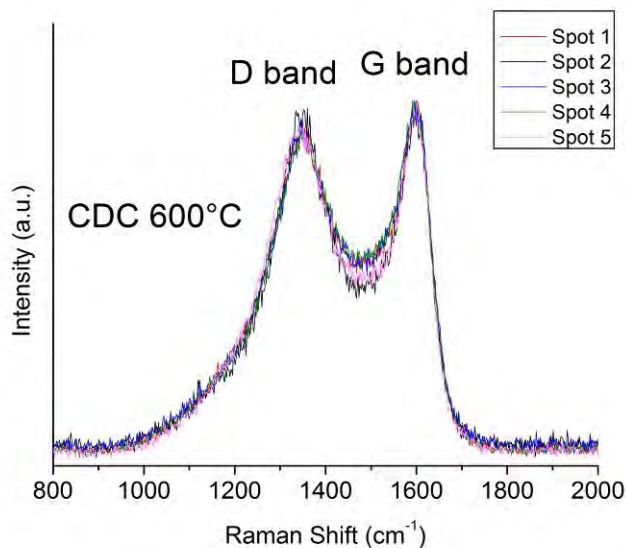


Figure 20. Raman Spectra of TiC CDC 600°C taken at five random sample spots. Raman spectra were recorded using 514 nm laser excitation.

The Raman spectra recorded at five random sample spots show similar D/G ratios, indicating a homogenous sample composition. Spectra exhibit a broad D-band feature and D/G ratios around ~1.0 (D and G bands have equal intensities), suggesting a highly amorphous nature. This is in good agreement with the results obtained from XRD analysis.

Figure 21 shows the Raman spectra recorded from TiC-CDC 1000°C.

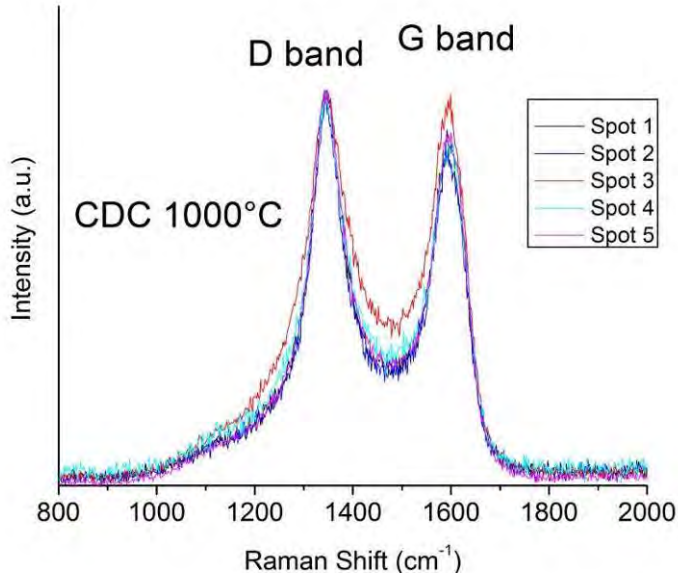


Figure 21. Raman Spectra of TiC-CDC 1000 °C taken at five random spots on the sample.

In analogy to TiC-CDC 600°C, measurements were taken at five random spots across the sample and were normalized with respect to the maximum intensity, in this case the D band. The D band intensity is higher with respect to the G band intensity (higher D/G ratio) when compared to TiC-CDC 600°C. At first, this does not make sense since the ordering of TiC-CDC 1000°C is higher than that of TiC-CDC 600°C. However, when considering the origin of the D band from a molecular point of view, the observed changes are in good agreement with XRD results. The D band results from the breathing vibrations of the hexagonal  $sp^2$  rings, but is Raman forbidden under normal conditions. However, in the presence of defects and disorder, the D band mode becomes Raman active and appears in the Raman spectrum of carbon materials. Therefore, the presence of the D band requires the existence of both hexagonal rings and lattice defects. As structural order increases with increasing synthesis temperature (from 600 to 1000°C), more rings are formed and the D band intensity increases. This is good agreement with XRD results. In addition, the Raman peaks of TiC-

CDC 1000°C are more narrow as compared to TiC-CDC 600°C, which is another indicator for the higher structural ordering. Unlike in TiC-CDC 600°C, spectra recorded from different areas exhibit variations with respect to the D and G band intensities and peak widths, suggesting larger inhomogeneities in the composition of the TiC-CDC 1000°C sample due to different areas exhibiting lower and higher graphitization.

Figure 22 shows the Raman spectra of TiC-CDC 1200°C recorded at five random spots within the sample. Spectra were normalized with respect to the maximum G band intensity.

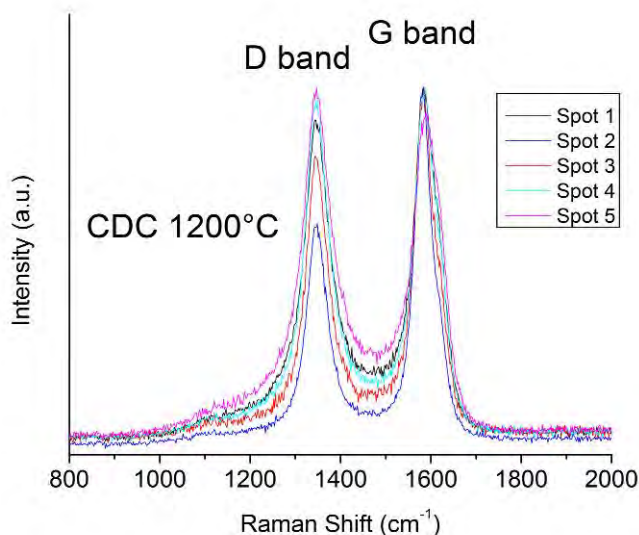


Figure 22. Raman Spectra of TiC-CDC 1200°C taken at five different random spots on the sample.

The Raman spectra of TiC-CDC 1200°C exhibit narrow D and G bands with D/G ratios ranging from ~1.2 to 0.6, suggesting a further increase in ordering compared to TiC-CDC 1000°C. The fluctuations in D/G indicate substantial inhomogeneity in sample composition due to more pronounced variations in level of graphitization. When increasing the chlorination temperature from 1000 to 1200°C, the D/G ratio increases primarily due to an increase in G band intensity.

Figure 23 shows a direct comparison of the Raman spectra of TiC-CDC synthesized at 600, 1000, and 1200°C. Each spectrum represents an average value for the respective sample.

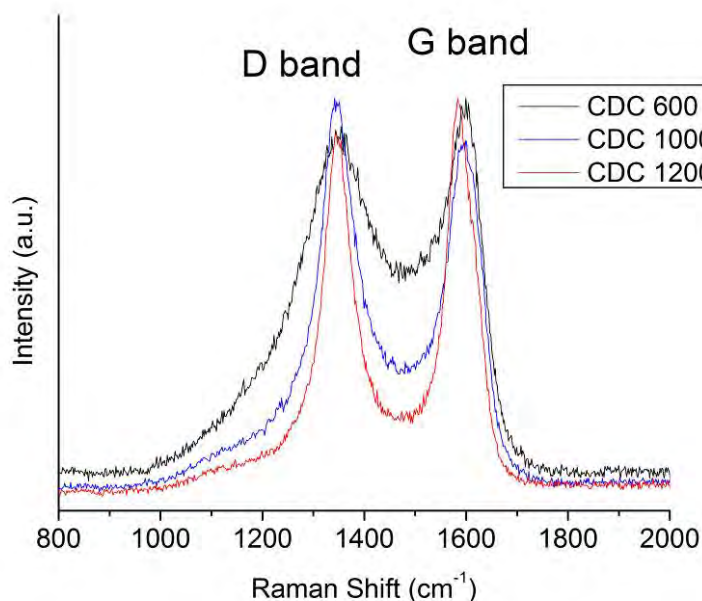


Figure 23. Raman Spectra of TiC-CDC 600, 1000, and 1200 °C. The peak width of the D and G bands decreases with increasing synthesis temperature indicating higher order and graphitization.

The graph summarizes the changes in the Raman spectra as the chlorination temperature increases from 600 to 1200°C. Highly amorphous TiC-CDC 600°C shows broad D and G bands with a D/G ratio slightly below one. With increasing synthesis temperature, ordering and graphitization increase, leading to narrower Raman bands as in the case of TiC-CDC 1000°C. The D/G ratio increases due to the formation of hexagonal rings and the related increase in D band intensity. A further increase in synthesis temperature (TiC-CDC 1200°C) leads to a continued reduction in line width of the D and G bands and a decrease in D/G. The increasing D/G ratio results from an increase in G band intensity due to higher levels of graphitization. The inhomogeneity of the samples

also increases with increasing temperature, suggesting non-uniform graphitization reactions during chlorination.

### 3. Scanning Electron Microscopy

Scanning electron microscopy (SEM) images were recorded from two fabricated TiC-CDC electrodes. Figure 24 shows the SEM images taken from a) TiC-CDC 600°C and b) TiC-CDC 1000°C electrodes at 500X magnification.

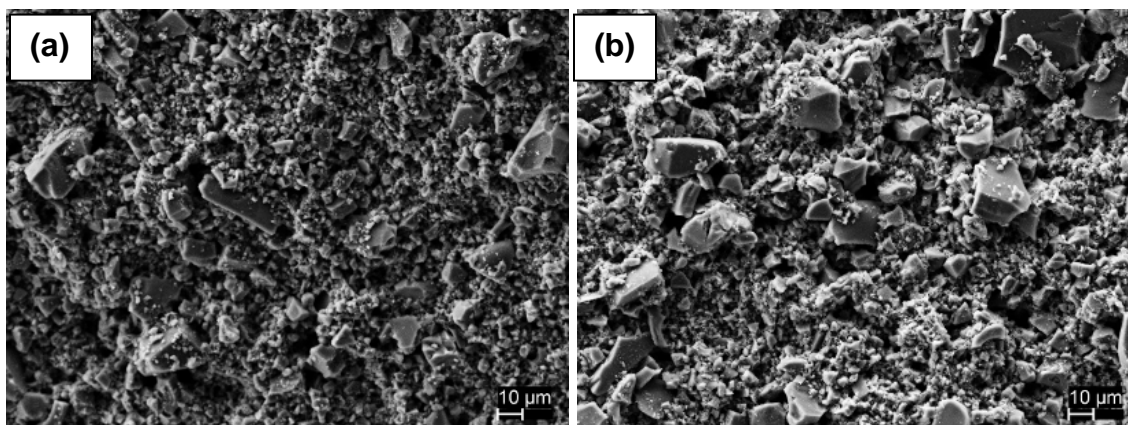


Figure 24. SE SEM images of TiC-CDC 600°C (a) and TiC-CDC 1000°C (b) electrodes at a magnification of 500X.

Both samples show similar microstructures and particle sizes. The particle size ranges from less than 1  $\mu\text{m}$  to about 50  $\mu\text{m}$ . Higher magnification images (5000X) reveal the polygonal nature of the particles (Figure 25). A further increase in magnification to 25,000X (Figure 26) reveals that the CDC particles are coated with the PVDF binder; however, the coating is not homogeneous but rather intermittent in form of millions of nanometer-sized droplets sparsely distributed over the particle surface. This non-uniform binder coverage reduces the mechanical stability of the electrode and may explain the flaking and cracking observed during the electrode casting process. While the amount of PVDF (15 wt%) used for CDC anodes was large compared to commercial electrodes (~5 wt%), the total surface area of CDC is more than 10 times higher than that of graphitic powders and may require additional processing for optimal stability.

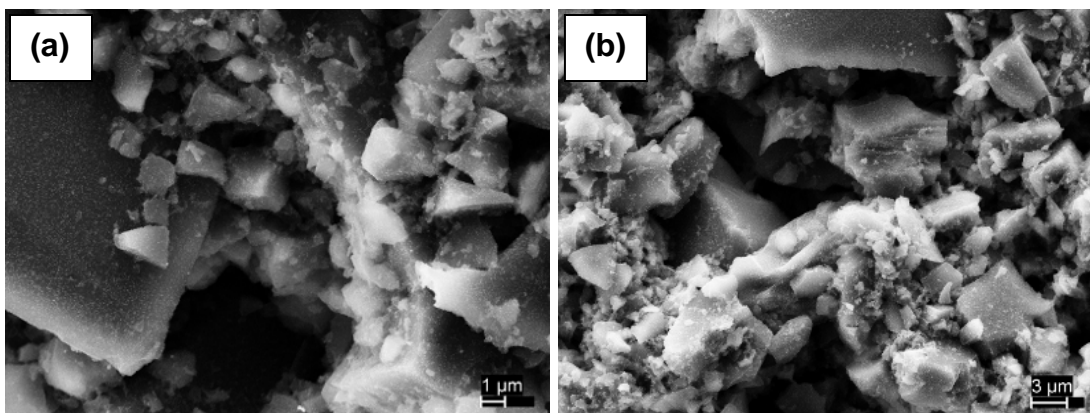


Figure 25. SE SEM images of TiC-CDC 600°C (a) and TiC-CDC 1000°C (b) electrodes at a magnification of 5000X.

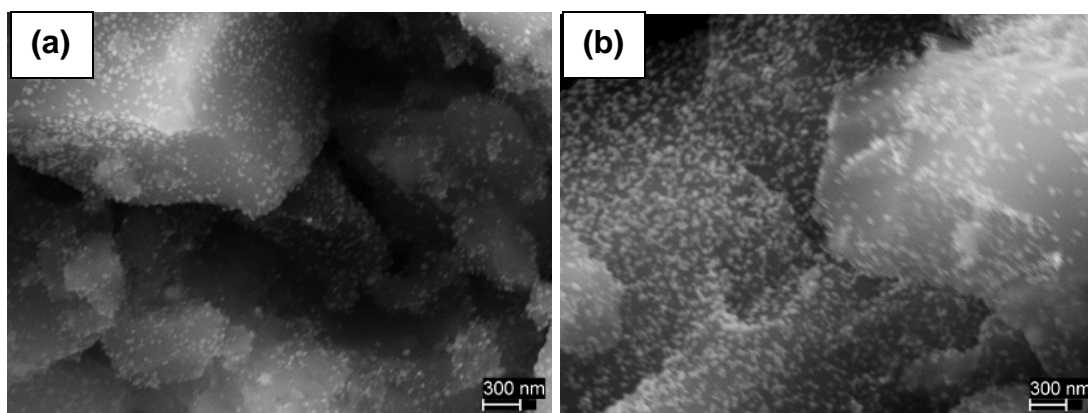


Figure 26. SE SEM images of TiC-CDC 600°C (a) and TiC-CDC 1000°C (b) electrodes at a magnification of 25kX.

### C. ELECTRODE AND BATTERY TESTING

Eight different types of button-type Li-ion coin cell batteries were constructed and tested using NPS's Maccor 4200 battery test system. The cells consisted of either commercial graphite or TiC-CDC (600, 1000, and 1200°C) anodes and commercial LiCoO<sub>2</sub> or lithium metal cathodes.

First, cells comprising commercial anode and cathode materials were tested in order to determine the effects of the cell assembly process on cell performance. Since the performance metrics of the commercial electrodes is

known, any difference between reported and measured values must be ascribed to the assembly process. In the second part of the electrochemical testing, three different types of CDC anodes were evaluated using CDC/Li metal half-cells and CDC/LiCoO<sub>2</sub> batteries.

### **1. Graphite Anodes**

Figure 27a and 27b show the time-dependent voltage of a graphite/LiCoO<sub>2</sub> coin cell during the first and fifth charge/discharge cycle, respectively.

LiCoO<sub>2</sub>-based Li-ion batteries are commonly cycled between 3 and 4.2 V. The charge rate, also known as C-rate, refers to the current that is needed to charge or discharge the battery within one hour. For example, if a battery has a total capacity of 1000 mAh, then a C-rate of 1C corresponds to a charge/discharge current of 1000 mA, whereas C-rates of 2C and C/2 refer to charge/discharge currents of 2000 mA and 500 mA, respectively. The charge (discharge) capacity of the battery is determined by the product of charging (discharging) time and charge (discharge) current. Since the current is constant during charge (discharge), the charging (discharging) times shown in Figure 28 are directly proportional to the charge (discharge) capacities.

Figure 28 displays the corresponding specific charge and discharge capacities as a function of the cycle number. The specific capacities shown in this graph represent the total capacity of the coin cell battery (measured), normalized by the weight of the active cathode material (LiCoO<sub>2</sub>). The fabricated cells have an excess of anode material and thus anode capacity. The total capacity of the cell is therefore limited by the capacity of the cathode.

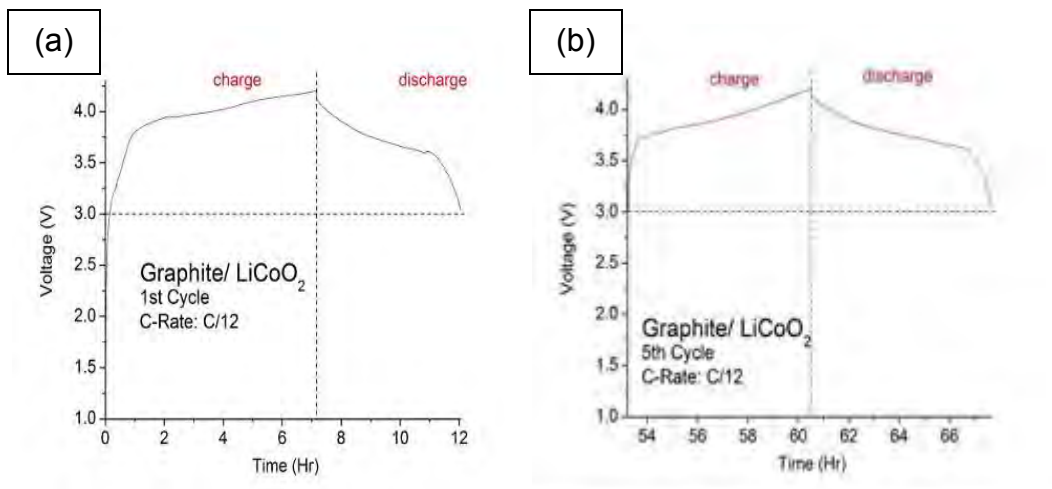


Figure 27. Charge and discharge behavior of a graphite/  $\text{LiCoO}_2$  coin cell during the (a) first and (b) fifth cycles. The charge and discharge current was 0.361 mA, which corresponds to a C-rate of  $\sim\text{C}/12$ .

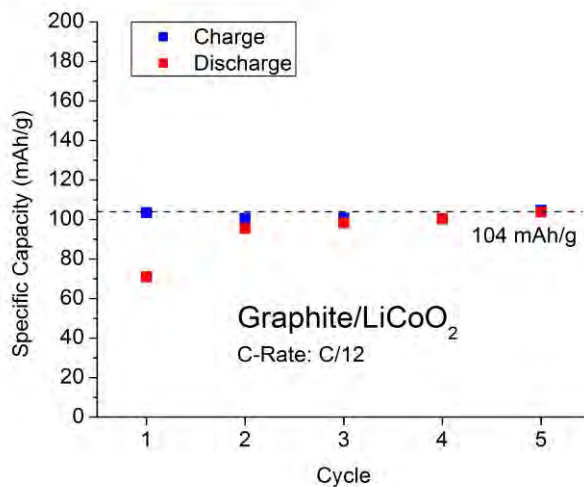


Figure 28. Specific charge and discharge capacities of a graphite/  $\text{LiCoO}_2$  coin cell during the first five cycles. The charge and discharge current was 0.36 mA ( $\text{C}/12$ ).

The difference between specific charge and discharge capacity during the first cycle (Figure 27a) is due to the formation of the solid electrolyte interphase (SEI) layer. The specific charge capacity reaches  $\sim 105$  mAh/g in the first cycle,

while the specific discharge capacity is considerably lower (~70 mAh/g). After a few cycles, the SEI layer is stabilized, and specific charge and discharge capacities reach similar values. The formation of the SEI layer is characteristic to the first cycle of Li-ion batteries. Lithium ions are consumed by a variety of chemical reactions and are incorporated into a passivation film (SEI layer). This process is irreversible and therefore denotes a loss of capacity, commonly referred to as irreversible capacity. The magnitude of the irreversible capacity depends on the nature of the electrode material, specifically the type of carbon used for the anode as well as the electrolyte formulation [2]. After the initial 2–3 cycles, charge and discharge capacities eventually balance out, reaching approximately 100 mAh/g. The practical specific capacity of the LiCoO<sub>2</sub> cathode, as reported by the manufacturer, is 145 mAh/g.

It should be noted that when prototype anodes and cathodes are prepared in the laboratory, the mass of the active material is determined precisely, whereas the volume is an estimate based upon an approximate tap density. Therefore, it is more scientifically rigorous to speak in terms of specific capacity and specific energy, which are derived from a measured charge and voltage, normalized by a well-known mass. In contrast, the energy density of the electrodes is normalized by the electrode volume.

Figure 29 shows the specific charge and discharge capacities of the same graphite/LiCoO<sub>2</sub> coin cell, measured using different charge and discharge rates.

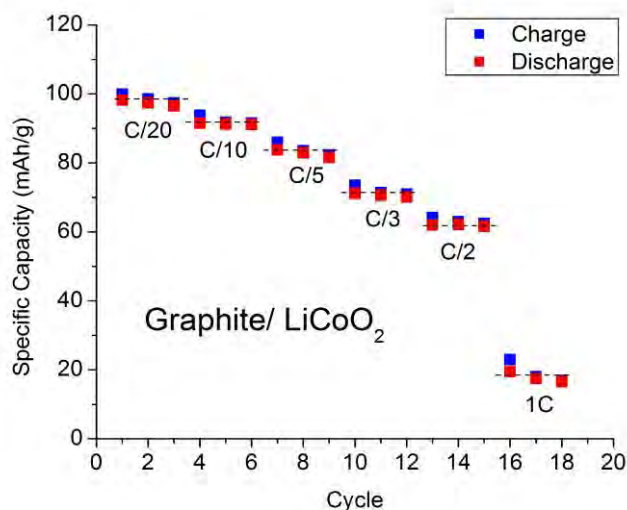


Figure 29. Specific charge and discharge capacities of a graphite/ LiCoO<sub>2</sub> coin cell at difference charge/discharge rates (rate testing). A C-rate of 1C corresponds to a current of 4mA.

The battery was cycled three times at six different C-rates: C/20, C/10, C/5, C/3, C/2, and 1C. With increasing charge/discharge rates, the specific capacities decrease from ~100 mAh/g at C/20 to ~20 mAh/g at 1C. This effect is well known and ascribed to mass transport limitations at the electrodes [2]. The capacity plot in Figure 30 does not exhibit any signs of SEI layer formation since the battery was already cycled before rate testing.

In next series of experiments, charge/discharge cycling data was collected from a graphite/Li metal half-cell. Figure 30 displays the cell voltage as a function of time during charge and discharge in the first (Figure 30a) and fifth (Figure 30b) cycle. Because the LiCoO<sub>2</sub> cathode has been replaced with Li metal, the voltage range during cycling is -3.0 V to 0 V vs. Li/Li<sup>+</sup> [4].

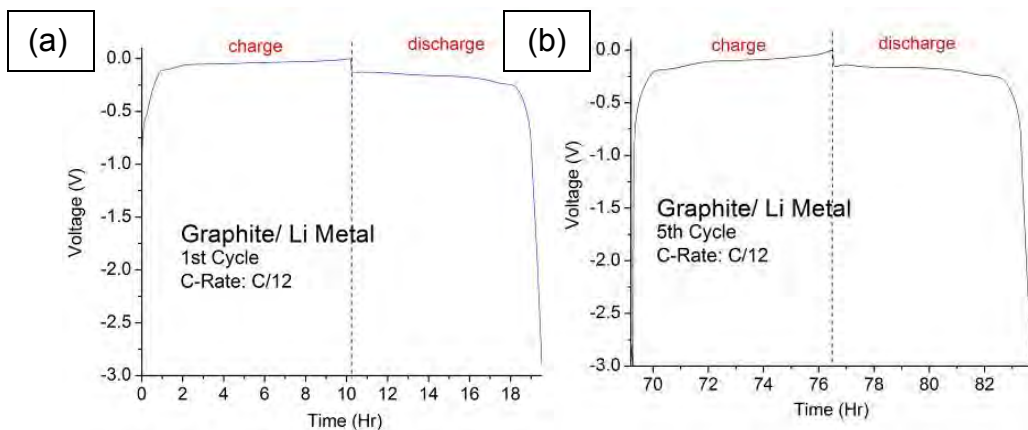


Figure 30. Cell voltage of a graphite/ Li metal coin cell during charge and discharge in the first (a) and fifth (b) cycles. The cell was charged and discharge at current of 0.361 mA (C/12).

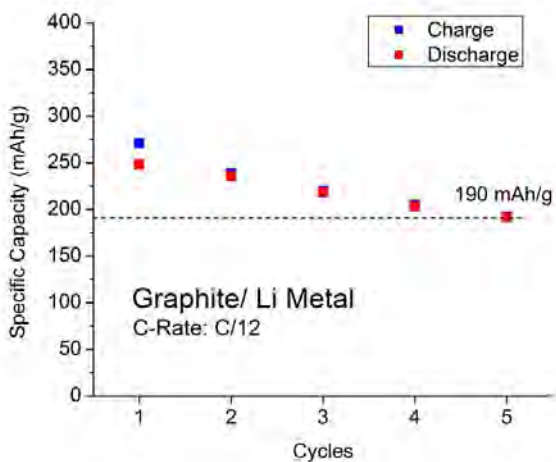


Figure 31. Specific charge and discharge capacity of graphite/ Li Metal half-cell as a function of cycle number. The charge and discharge current was set to 0.36 mA (C/12).

The graphite/Li metal half-cell shows a flat voltage profile for most of the charge and discharge, which is characteristic to the intercalation and deintercalation process of graphite. In contrast, the voltage profile of the graphite/LiCoO<sub>2</sub> (Figure 27) exhibits a continuous slope during charge and discharge, due to additional contributions from lithiation/delithiation processes at the cathode.

The corresponding specific capacities are shown in Figure 31. Due to the excess of lithium, the capacity of the half-cell is limited by the capacity of the graphite anode. The first cycle exhibits an irreversible specific capacity of ~25 mAh/g due the SEI layer formation at the graphite anode (Figure 31), similar to the graphite/LiCoO<sub>2</sub> cell.

Upon cycling, the specific discharge capacity decreases from ~250 mAh/g after the first cycle to ~190 mAh/g after the fifth cycle. The practical specific capacity of the graphite anode, as reported by the manufacturer, is 330 mAh/g. Figure 33 shows the specific charge and discharge capacities of a graphite/Li metal half-cell during rate testing at six different currents (C-rates).

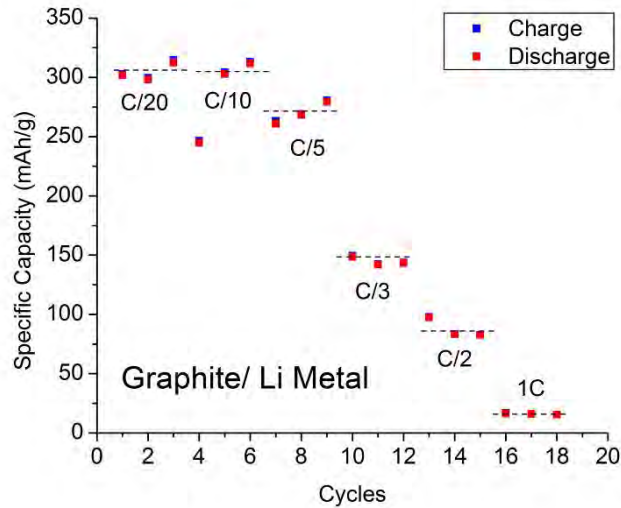


Figure 32. Specific charge and discharge capacities of a graphite/ Li metal coin cell at difference charge/discharge rates (rate testing). A C-rate of 1C corresponds to a current of 4 mA.

The specific charge and discharge capacities at C/20 measure between 300–315 mAh/g, but drop to ~150 mAh/g at C/3 and to 16 mAh/g at 1C. The graphite anode exhibits high specific capacities of >250 mAh/g, but is subject to lower specific capacities at high charge and discharge currents (> C/5), revealing the power limitations of graphite-based Li-ion battery anodes.

## 2. Carbide-Derived Carbon Anodes

In the second part of the test series, TiC-CDC anodes (600, 1000, and 1200°C) were cycled versus Li metal and LiCoO<sub>2</sub> cathodes.

The time-dependent voltage profile of a TiC-CDC 600/LiCoO<sub>2</sub> coin cell during charge and discharge at C/5 is shown in Figure 33. The corresponding specific charge and discharge capacities are given in Figure 34. The first cycle exhibits a specific charge capacity of 730 mAh/g, but only ~35 mAh/g are retrieved upon discharge, suggesting an irreversible capacity of 695 mAh/g. Due to the large surface area (BET-SSA of up to 3000 m<sup>2</sup>/g) CDC consumes the majority of the available Li ions during SEI layer formation in the first cycle. Since the total number of Li ions in the cell is given by the capacity of the cathode and cannot be replenished, the discharge capacity remains low (<40 mAh/g) in the following cycles. As shown in Figure 34, the specific charge capacity is slightly higher than the discharge capacity of the previous cycle. This may be explained by the fact that either not all of the accessible Li is removed from LiCoO<sub>2</sub> in the first cycle, or that other non-lithium-consuming, irreversible redox reactions occur upon charge and therefore contribute to the specific charge capacity.

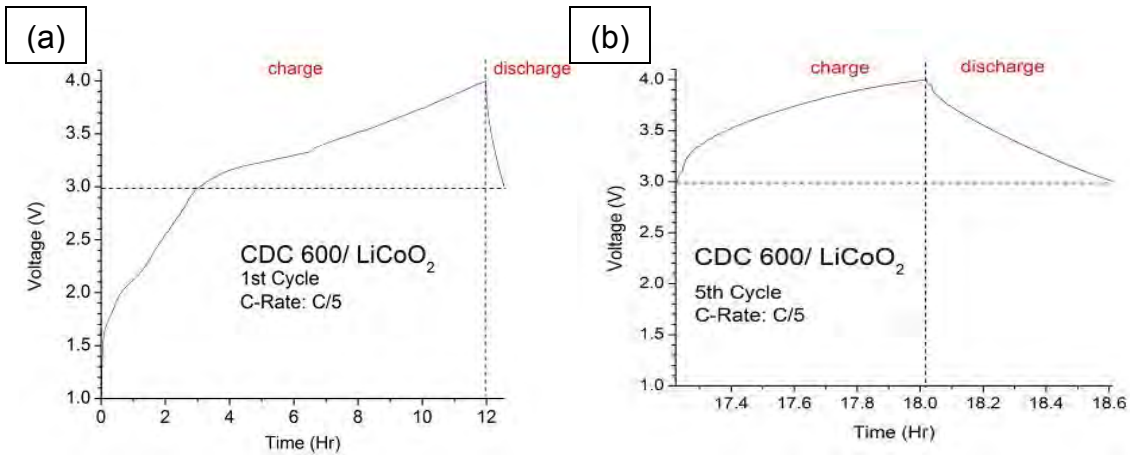


Figure 33. Cell voltage of a TiC-CDC 600°C/LiCoO<sub>2</sub> coin cell during charge and discharge in the first (a) and fifth (b) cycles. The cell was charged and discharge at current of 0.30 mA (C/5).

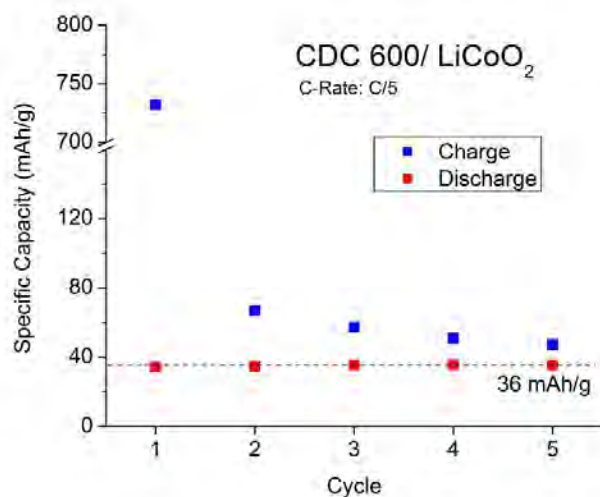


Figure 34. Specific charge and discharge capacity of a TiC-CDC 600°C/LiCoO<sub>2</sub> coin cell as a function of cycle number. The charge and discharge current was set to 0.30 mA (C/5).

The charge and discharge voltage profiles of a TiC-CDC 600°C/Li metal half-cell are shown in Figure 35. The half-cell is cycled between -3.0 and 0V. Similar to the TiC-CDC 600°C/LiCoO<sub>2</sub> battery, the TiC-CDC 600°C/Li metal half-cell is subject to a large irrepressible capacity during the first cycle (Figure 35a). Unlike graphite (Figure 30), TiC-CDC 600°C does not undergo conventional intercalation/deintercalation reactions and exhibits a continuously sloping voltage profile during charge and discharge.

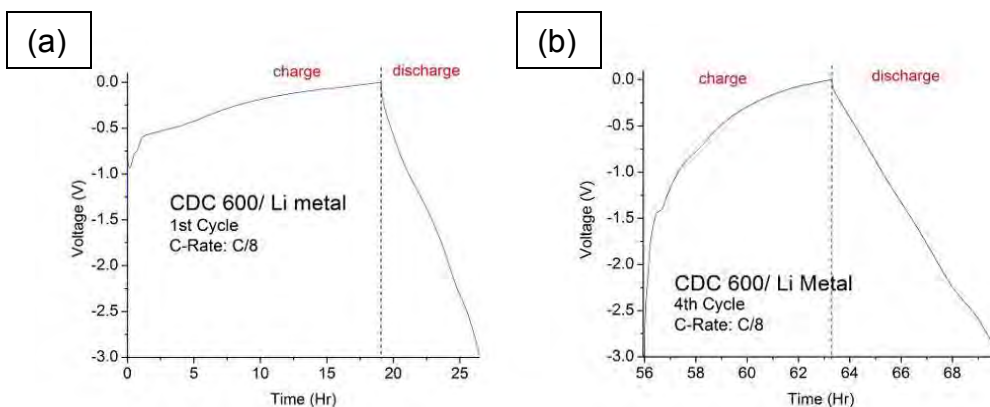


Figure 35. Cell voltage of a TiC CDC 600°C/Li metal coin cell during charge and discharge in the first (a) and fourth (b) cycles. The cell was charged and discharge at current of 0.30 mA (C/8).

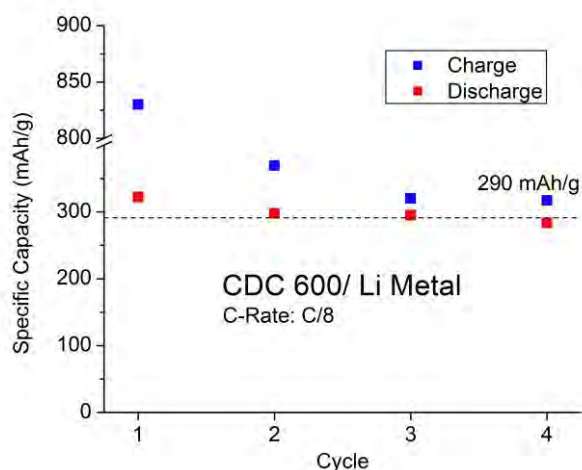


Figure 36. Specific charge and discharge capacity of a TiC CDC 600°C/Li metal coin cell as a function of cycle number. The charge and discharge current was set to 0.30 mA (C/8).

Figure 36 shows the corresponding specific charge and discharge capacities as a function of the cycle number. After four cycles, the specific capacity approaches ~290 mAh/g

To evaluate the consistency in cell fabrication and reproducibility of the test results, a second TiC-CDC 600°C/Li metal cells was constructed and cycled more than 50 times (Figure 38).

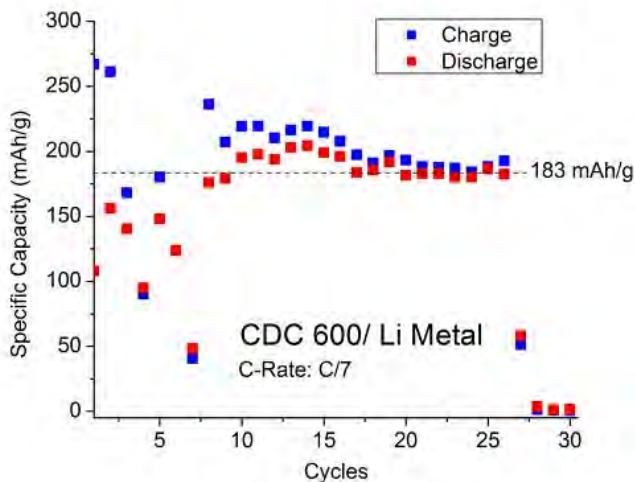


Figure 37. Specific charge and discharge capacity of a TiC CDC 600°C/Li metal coin cell as a function of cycle number. The charge and discharge current was set to 0.30 mA (C/7).

The specific charge and discharge capacities show large fluctuations in during first 7–8 cycles, with specific discharge capacities ranging from of ~40 mAh/g to ~180 mAh/g. While the origin of these fluctuations remains unknown, the results demonstrate the need for further improvements in both the electrode fabrication and the cell assembly. The specific discharge capacity increases to around 210 mAh/g during the 13th and 14th cycle, and reaches an average value of 185 mAh/g until an abrupt cell failure in the 28th cycle.

Figure 38 shows the cell voltage a TiC-CDC 1000°C/Li metal half-cell during charge and discharge and in the first (Figure 38a) and fifth (Figure 38b) cycle. The voltage profile is similar to that obtained for the TiC-CDC 600°C; however, the specific charge and discharge capacities were found to be slightly lower, reaching an average specific discharge capacity of 275 mAh/g after the fourth cycle.

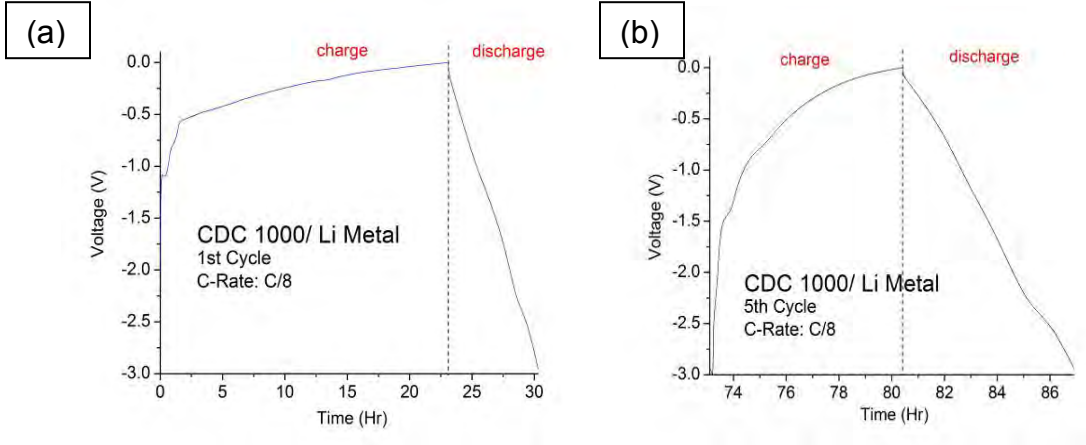


Figure 38. Cell voltage of a TiC-CDC 1000°C/Li metal coin cell during charge and discharge in the first (a) and fifth (b) cycles. The cell was charged and discharge at current of 0.30 mA (C/8).

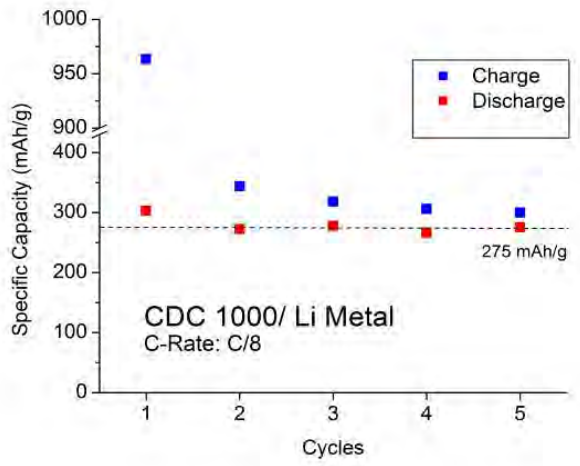


Figure 39. Specific charge and discharge capacity of a TiC-CDC 1000°C/ Li metal coin cell as a function of cycle number. The charge and discharge current was set to 0.30 mA (C/8).

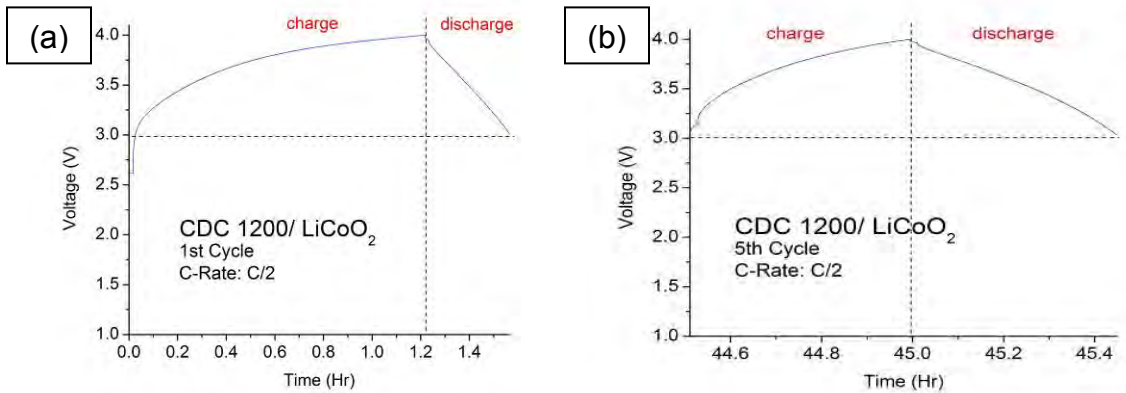


Figure 40. Cell voltage of a TiC-CDC 1200°C/LiCoO<sub>2</sub> coin cell during charge and discharge in the first (a) and fifth (b) cycles. The cell was charged and discharge at current of 0.30 mA (C/2).

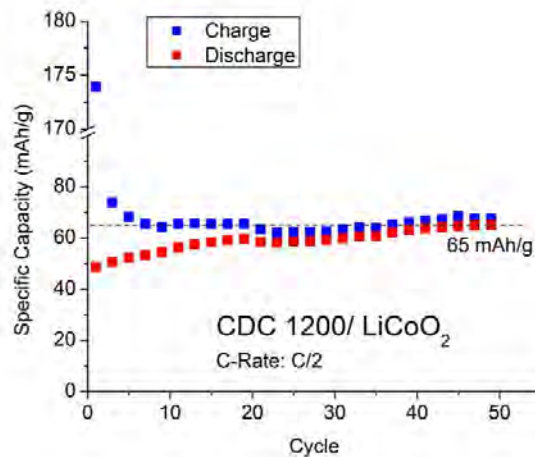


Figure 41. Specific charge and discharge capacity of a TiC-CDC 1200°C/ LiCoO<sub>2</sub> coin cell as a function of cycle number. The charge and discharge current was set to 0.30 mA (C/2).

The voltage profile of a TiC-CDC 1200°C/LiCoO<sub>2</sub> coin cell during charge and discharge in the first (a) and fifth (b) cycle is given in Figure 41. As expected, TiC-CDC 1200°C exhibits a large irreversible capacity during the first cycle due to SEI layer formation (Figure 41a). Figure 42 displays the corresponding specific charge and discharge capacities. The cell has been successfully cycled for more than 50 cycles, showing an average specific discharge capacity of 65

mAh/g at the 50<sup>th</sup> cycle. While at first glance, the specific capacity appears considerably lower than that of the graphite/LiCoO<sub>2</sub> cells, the TiC-CDC 1200°C/LiCoO<sub>2</sub> coin cell was cycles at a rate of 1C, should therefore be compared with the specific capacity values that were measured at high C-rates. In the case of graphite/LiCoO<sub>2</sub>, specific discharge capacities at 1C were less than 20 mAh/g, which is more than 3 times lower than the values obtained for TiC-CDC 1200°C/LiCoO<sub>2</sub>, suggesting that CDCs indeed exhibit superior power characteristic as compared to graphite electrodes.

Figures 42 and Figure 43 show the voltage profile and specific capacities of a TiC CDC 1200°C/Li metal half-cell, respectively.

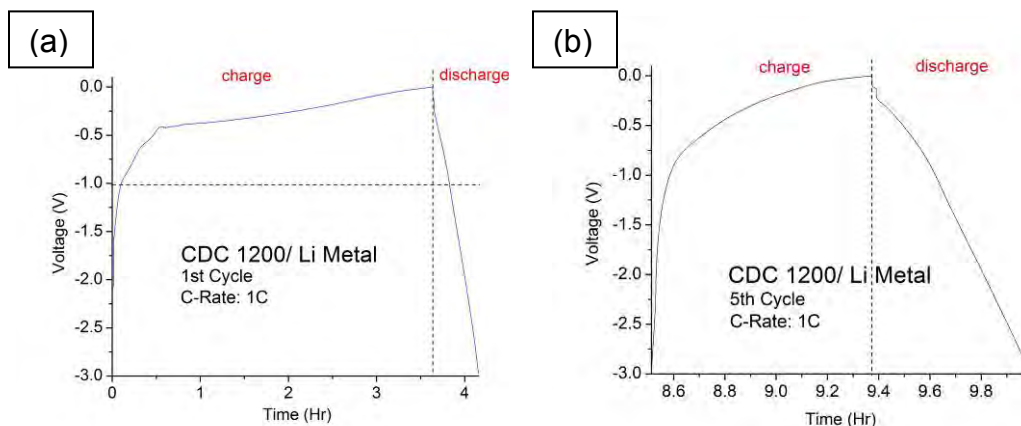


Figure 42. Cell voltage of a TiC-CDC 1200°C/Li metal half-cell during charge and discharge in the first (a) and fifth (b) cycles. The cell was charged and discharge at current of 0.30 mA (1C).

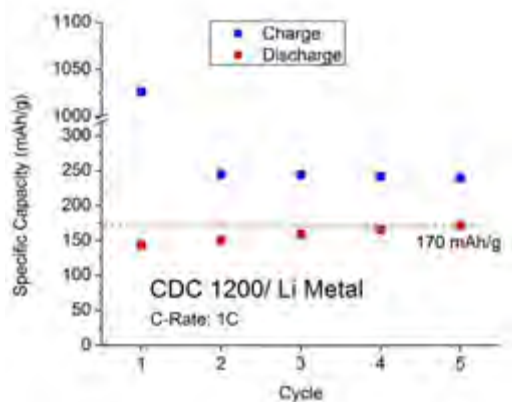


Figure 43. Specific charge and discharge capacity of a TiC-CDC 1200°C/ Li metal half-cell as a function of cycle number. The charge and discharge current was set to 0.30 mA (1C).

Similar to TiC-CDC 600°C and TiC-CDC 1000°C, TiC CDC 1200°C is subject to a large irreversible capacity in the first cycle (Figures 42a and 43). The specific discharge capacity reaches ~170 mAh/g in the fifth cycle. Again, it should be noted that this cell was cycled at 1C. The equivalent specific discharge capacity (at 1C) of the graphite/Li metal half-cell is 16 mAh/g, more than 10 times lower than the value measured for TiC-CDC 1200°C. Therefore, while the specific capacities of the CDC samples remain below the values measured for graphite anodes, the power characteristics of TiC-CDC 1200°C far exceed the performance of conventional graphite anodes.

THIS PAGE INTENTIONALLY LEFT BLANK

## IV. SUMMARY AND CONCLUSIONS

The results presented in this thesis mark the first battery research efforts at NPS. Substantial progress was made in establishing fabrication processes and installing state-of-the-art testing facilities, both of which lay the foundation for groundbreaking future energy research at NPS.

In the scope of this thesis, we developed, implemented, and optimized a multistep electrode fabrication process that can be used to prepare conventional and customized Li-ion battery anodes and cathodes at NPS. In addition, we installed, calibrated, and tested several state-of-the-art battery testing facilities, providing new energy research capabilities to NPS.

Using conventional anode and cathode materials, we successfully fabricated, characterized, and tested several self-made electrodes and Li-ion coin cell batteries. The measured specific capacities were found to be lower than the values reported by the manufacturer, suggesting that further optimization of the fabrication process is needed in future studies.

After small adjustments to the fabrication process, three different types of CDC anodes were built, consisting of TiC-CDC synthesized at 600, 1000, and 1200 °C. X-ray diffraction (XRD), Raman spectroscopy, and scanning electron microscopy (SEM) were used to evaluate both the level of graphitization and the microstructure of the CDC electrodes. Material characterization revealed the highly amorphous nature of TiC-CDC 600°C and showed an increase in ordering and graphitization with increasing synthesis temperature, as expected.

The fabricated TiC-CDC anodes were tested and successfully cycled against Li metal (half-cell) and LiCoO<sub>2</sub> cathodes. Due to their large surface area and the related SEI layer formation, all TiC-CDC exhibited high irreversible capacities in the first charge/discharge cycle. The specific discharge capacities of the TiC-CDC/LiCoO<sub>2</sub> coin cells were low (<80 mAh/g) since the majority of the available lithium was consumed by the formation of SEI layer during the first

charge. In contrast, TiC-CDC/Li metal half-cells revealed specific capacities up to 290 mAh/g. While the half-cells were subject to similar irreversible capacities, the lithium metal electrode provided an excess of lithium and allowed for continued cycling with high charge and discharge capacities.

Highly amorphous TiC-CDC 600°C demonstrated the highest specific capacity of ~290 mAh/g, while the more ordered TiC-CDC 1000°C and TiC-CDC 1200°C samples exhibited specific capacities of 275 mAh/g, and 170 mAh/g, respectively. These results show an increase in specific capacity with decreasing structural ordering, suggesting that less ordered CDCs, synthesized at chlorination temperatures of 600 °C and below, are more suitable for Li-ion battery electrodes.

TiC-CDC 1200°C revealed a specific discharge capacity of ~170 mAh/g at a discharge rate of 1C. The equivalent specific discharge capacity (at 1C) of the graphite/Li metal half-cell is 16 mAh/g, more than 10 times lower than the value measured for TiC CDC 1200°C. Although the average specific capacities of the CDC samples remain below the values measured for graphite anodes, the power characteristics of TiC-CDC 1200°C far exceed the performance of conventional graphite anodes.

While the obtained results on TiC-CDC are promising, additional studies are needed to determine the relationship between the various structural features of CDC and its electrochemical performance. In particular, further improvement of the fabrication process is required to achieve higher consistency and reproducibility in the electrochemical performance of the coin cell electrodes. Proposed future research includes the study of the effect of ball milling on the total surface area of TiC-CDC and the distribution of the PVDF binder. Required optimization steps are the standardization of the drying process and the electrolyte supply.

## LIST OF REFERENCES

- [1] C. Liu, L. Feng, L. Ma, H. Cheng. "Advanced materials for energy storage," *Advanced Energy Materials*, vol. 22, pp. E28-E62, 2010.
- [2] D. Linden and T. B. Reddy, *Handbook of Batteries*, 3rd. New York: McGraw-Hill, 2002.
- [3] Woodbank Communications Ltd. "Ragone plot." Internet: <http://www.mpoweruk.com/performance.htm>, 2005 [Sep. 1, 2011].
- [4] J. Farmer, S. Osswald, L. Brewer, et al., ME4901, "*Special Topics in Energy Conversion & Storage*," LLNL-MI-464396, LLNL, Livermore, CA, 2010.
- [5] J. M. Tarascon, M. Armand. "Issues and challenges facing rechargeable lithium batteries," *Nature*, vol. 414, pp. 359–367, Nov. 2001.
- [6] S. Osswald, Q. Hu, Y. Zhu, S.A. Wesel, R. Daniel, L. Ortiz, D.R. Sadoway. "Advanced lithium-ion batteries for high-temperature energy storage," *Materials Science and Technology*, vol. 196, pp. 5604–5610, Oct. 2009.
- [7] M. Noel, V. Suryanarayanan. "Role of carbon host lattices in Li-ion intercalation/ de-intercalation processes," *Journal of Power Sources*, vol. 111, pp. 193–209, May 2002.
- [8] M. Endo, C. Kim, K. Nishimura, T. Fujino, K. Miyashita. "Recent development of carbon materials for Li-ion batteries," *Carbon*, vol. 38, pp. 183–197, Jun. 1999.
- [9] H. Li, Z. Wang, L. Chen, X. Huang. "Research on advanced materials for Li-ion batteries," *Advanced Materials*, vol. 21, pp. 4593–4607, 2009.
- [10] R. Dash, J Chmiola, G. Yushin, Y. Gogotsi, G. Laudisio, J. Singer, J. Fischer, S. Kucheyev. "Titanium carbide derived nanoporous carbon for energy-related applications," *Carbon*, vol. 44, pp. 2489–2497, Apr. 2006.
- [11] G. Yushin, A. Nikitin, Y. Gogotsi. "Carbide-derived carbon," *Nanomaterials Handbook*, Philadelphia: CRC Press, 2006.
- [12] V. Presser, M. Heon, Y. Gogotsi. "Carbide-derived carbons – from porous networks to nanotubes and graphene," *Advanced Functional Materials*, vol. 10, pp. 1–24, 2011.

- [13] G. N. Yushin, E. N. Hoffman, A. Nikitin, H. Ye, M. W. Barsoum, Y. Gogotsi. "Synthesis of nanoporous carbide-derived carbon by chlorination of titanium silicon carbide," *Carbon*, vol. 43, pp. 2075–2082, Mar. 2005.
- [14] C. Suryanarayana and M. G. Norton, *X-Ray Diffraction A Practical Approach*. New York: Plenum Press, 1998.
- [15] B. L. Gabriel, *SEM: A User's Manual for Materials Science*. Metals Park, OH: American Society For Metals, 1985.
- [16] H. A. Szymanski, *Raman Spectroscopy Theory and Practice*. New York: Plenum Press, 1967.

## INITIAL DISTRIBUTION LIST

1. Defense Technical Information Center  
Ft. Belvoir, Virginia
2. Dudley Knox Library  
Naval Postgraduate School  
Monterey, California
3. Sebastian Osswald  
Naval Postgraduate School  
Monterey, California
4. Joseph Farmer  
Lawrence Livermore National Laboratory  
Livermore, California &  
Naval Postgraduate School  
Monterey, California